International Journal of Mechanical Sciences 244 (2023) 108078

Contents lists available at ScienceDirect

International Journal of Mechanical Sciences

journal homepage: www.elsevier.com/locate/ijmecsci

Hydrodynamic forces in non-uniform cantilever beam resonator

Lalsingh Devsoth, Ashok Kumar Pandey *

Department of Mechanical and Aerospace Engineering, Indian Institute of Technology Hyderabad, Kandi, Sangareddy, 502284, Telangana, India

ARTICLE INFO

Keywords:
Non-uniform beam
Hydrodynamic force
Boundary element method (BEM)
Fluid–structure interaction (FSI)

ABSTRACT

In this paper, we developed two dimensional and three dimensional boundary element method (BEM) to compute hydrodynamic forces due to the oscillation of non-uniform beam (NUB) in a quiescent incompressible fluid with linear and quartic varying widths. To model the fluid flow under small amplitude oscillation of thin NUB in its first mode, the linearized unsteady Stokes equation is solved using BEM. After finding the converged structural and fluid nodes in all the cases, we compute real and imaginary components of hydrodynamic function. Subsequently, damping ratio or quality factor is found from energy dissipation due to drag forces mainly because of stress jumps across the thin beam thickness. Similarly, the frequency shift is found due to virtual added mass obtained from the mean hydrodynamic thrust force. The results are validated with existing literature and further analysis is done in terms of tapering parameter and index of non-uniform beam, and the corresponding aspect ratio and frequency parameters. Based on the analysis presented, it is found that quartic converging beam provides better quality factor and least added mass effect and it can be explored to design a cantilever based resonator operating in fluid with improved performance such as AFM probes. Thus, the new model developed for non-uniform beam can be useful to drag forces in other types of 2D and 3D beams.

1. Introduction

Most of the micro and nanoelectromechanical systems (MEMS/NEMS) based cantilever resonators such as pressure sensors [1,2], mass sensors [3–6], biosensors [7–11], atomic force microscopy (AFM) [12–17], and smart material based piezoelectric energy harvesting devices [18–24], etc., perform their operation in the presence of fluid. In turn, the dynamic characteristics of flexible cantilever beams are affected by the surrounding fluid due to the hydrodynamic drag and added mass effects. These factors are the result of the complex flow field generated due to the oscillation of the micro cantilever structure and is largely dependent on the frequency and amplitude of the vibrating structure. The drag force is directly proportional to the unsteady viscous layer $\delta_s \propto \sqrt{\nu/\omega}$ around the beam [25,26] which describes the velocity diffusion on the oscillating surface. Here, ν is the kinematic viscosity of the fluid, and ω is the angular frequency. As the oscillation frequency increases, it leads to the formation of a small viscous layer and more vortex shedding around the vibrating structure. To describe the dependence of oscillation amplitude, Keulegan–Carpenter (KC) number is defined as the ratio of 2π times the amplitude of oscillation to the characteristic length, i.e., width at the fixed end b_0 of cantilever beam. At an infinitesimal small KC [8,27], the hydrodynamic drag force is independent of the oscillation amplitude and the flow is governed by the unsteady Stokes equation. For the moderate KC, the vortex shedding [28] and flow separation around the structure occur [7,8,27,29–31]. Hence, the frequency and amplitude of oscillating structure in fluid influences the convective-driven flow and makes the fluid damping non-linear [32].

There have been studies focusing on computing hydrodynamic forces due to thin and uniform cantilever beams [33,34]. However, recent studies have started focusing on shapes other than uniform cantilever based resonators like slotted, paddle type, V-shaped [35] or triangular type, converging and diverging beams, and arrow-shaped [36–41] to improve the performance of probes in AFM in non-contact and taping modes in fluid environment [42]. Recently, we found that non-uniform micro-cantilever beams can be used to improve the bandwidth of MEMS resonators and energy harvesters [18,20,39,40]. Since there is no model available to compute hydrodynamic forces in non-uniform beams, we develop a 2D and 3D BEM model to compute the hydrodynamic forces due to flexural motion of non-uniform beams (NUBs) in the current paper. Subsequently, we present a detailed fluid-structural interaction of non-uniform beam in air with varying widths in order to further optimize the above devices.

Some of the primitive studies to compute hydrodynamic forces involve the computation of the unsteady drag force on the oscillating sphere [1] and infinitely long cylinder [25,43] with small amplitude using the linearized unsteady Stokes flow in (r, θ) domain. Zhang and Turner [44,45] developed drag force as a function of frequency for

* Corresponding author.
E-mail addresses: me17resch11006@iith.ac.in (L. Devsoth), ashok@mae.iith.ac.in (A.K. Pandey).

https://doi.org/10.1016/j.ijmecsci.2022.108078
Received 4 August 2022; Received in revised form 27 November 2022; Accepted 22 December 2022
Available online 28 December 2022
0020-7403/© 2022 Elsevier Ltd. All rights reserved.

a rigid cylinder with a different cross-sectional area. Subsequently, the computation of the hydrodynamic force on a long cylinder with elliptic section [26] has also been studied in the elliptical coordinate system [46] with Mathieu functions. To solve the above problems, Tuck [47] used the stream function-based two-dimensional boundary integral formulation for a long beam to evaluate the pressure jump and vorticity jump across the thin beam using the boundary element method (BEM) [25]. Brumley et al. [48] found exact theoretical and asymptotic solution for an infinite long rectangular cross-section cylinder with a varying thickness-to-width ratio and compared the solution with the infinitely thin beam approximation. In addition, Phan et al. [49] performed a numerical study showing a significant increase in hydrodynamic damping with increase in the thickness to width ratio. However, they did not see any noticeable change in added mass. Using the thin beam theory (TBT) to include the flexural effect of a uniform beam, Sader [12] obtained a complex hydrodynamic function for rectangular sections by least-square fitting. He also obtained an empirical formulation for the frequency response corresponding to the exact mode shape of the cantilever beam immersed in viscous fluid subjected to the thermal driving force. Subsequently, the semi-analytical model has been used to calibrate the spring constant of AFM cantilevers with different shapes by considering the complex hydrodynamic function [13,50,51]. Green et al. [15] obtained the semi-analytical model for hydrodynamic load per unit length to estimate the drag of an oscillating beam. The above studies are limited to long cantilever beam oscillating in fluid at various frequencies under small amplitude.

Since, the hydrodynamic forces are also affected due to the presence of nearby wall, the fluid damping consists of drag and squeeze film damping. Hanning et al. [3] analyzed the effect of nearby wall characterized by the air-gap on the hydrodynamic forces in a uniform beam. Rankl et al. [52] computed hydrodynamic forces in magnetically actuated cantilever beam near to the wall. Grimaldi et al. [53] approximately computed hydrodynamic forces in sharp edged cantilever near the wall. Ashok et al. [54] performed computational and experimental studies to compute quality factor and damping due to fluid in the presence of wall. They also studied the variation of wall-gap on the fluid damping. Vignola et al. [55] estimated the viscous damping in a micro-scale resonator for mass sensing. Basak et al. [36] used the finite element based three-dimensional fluid–structure interaction model for computing hydrodynamic forces for different structures like slotted type, paddle type, and triangular microcantilevers with and without proximity to another fixed surface. It was found that the damping, as well as added mass effects, increase as the oscillating surface moves closer to the fixed surface. Aureli et al. [7] performed an analysis on flexible rectangular beam oscillating in the fluid corresponding to an exact mode based on the Euler–Bernoulli beam theory and estimated that the non-linear hydrodynamic function depends on the oscillation amplitude and frequency parameter.

To demonstrate more control over hydrodynamic forces, Ahsan and Aureli [8,56] utilized BEM and finite volume method (FVM) to estimate linear and non-linear drag forces in two-dimensional shape morphed beam executing transverse and torsional oscillations in a viscous fluid. They found that the shape-morphed curvature reduces the hydrodynamic forces and, thus, minimizes the power dissipation significantly. Hosaka et al. [1] computed air-drag and other fluid damping by replacing the oscillating beam with a series of spheres along its length. Maali et al. [57] described the behavior of AFM long cantilever beam in air and water up to eight modes. Korayem et al. [58] carried out the modeling of AFM cantilever beams by considering the variation of torsional moment and shear with tilt angle, length of the probe, and fluid properties. Pozrikidis [59] used the singularity method to obtain the drag force on an oscillating spherical drop by solving the linear unsteady Stokes equation. Subsequently, he used BEM to compute hydrodynamic forces due to the oscillation of different particles such as spheroids, dumbbells, and biconcave discs in viscous fluid [60]. Loewenberg [61] utilized a boundary layer solution to obtain hydrodynamic forces due to the oscillation of finite-length cylinder for low to moderate oscillating frequencies.

Based on the Pozrikidis [59,60] and Loewenberg [61] models, few researchers have developed three-dimensional hydrodynamic forces. Clarke et al. obtained the hydrodynamic forces due to the rigid oscillation of titled circular cylinder [37] and rectangular plate [38] near the fixed wall using the three-dimensional boundary integral methods. Ahsan and Aureli [62] extended their two-dimensional problem to three-dimensional using boundary integral method to obtain hydrodynamic forces in a shape-morphed beam oscillating in its first mode. Farokhi and Ghayesh [63] described the nonlinear vibrations of a cantilever subjected to base excitation in primary and secondary resonance. Facci and Porfiri [19] solved the incompressible Navier Stokes equation using FVM (finite volume method) to obtain hydrodynamic damping and added-mass effects and compared the results with experiments. The thrust force generated along the axial direction of the beam is estimated due to the added mass force [4,64,65]. Vishwakarma et al. [66] compared the influence of drag and squeeze film damping as a function of beam width and air gap with respect to the fixed surface. They computed the drag force based on the oscillating disc and damping force obtained from the Reynolds equation. Ashok et al. [67] performed experimental studies to compute the variation of fluid damping and frequencies of non-uniform beams with linearly and quartic varying widths. In yet another study, Ashok et al. [40] performed analysis by solving incompressible Navier–Stokes equation in ANSYS to compute fluid damping in arrow-shaped beam. The results are also compared with experiments. All the models developed based on the submerged cantilever beam oscillation give pure hydrodynamic dissipation. The influence of the structural damping has also been studied on an oscillating cantilever beam in fluid [68]. Furthermore, Gesing et al. [34,69] performed an analysis on a micro-resonator with finite width and analyzed the effect of damping and added mass on flexural, torsional, and roof tile-shaped geometries with non-conventional vibration modes. Subsequently, to compute drag forces in an array of beams, many studies [70–72] employed two dimensional approach and performed hydrodynamic coupling analysis. Based on the above studies, we noticed that majority of the analytical and semi-analytical models are developed for long cylinders and uniform beams by solving steady as well as unsteady Stokes equation. They discussed the effect of amplitude, frequency of oscillation, and boundaries surrounding uniform cantilever beams to analyze hydrodynamic drag with 2D and 3D formulations. Thus, all the previous studies formulations were limited to uniform beams. Therefore, in this paper, we describe the procedure of developing semi-numerical approach to compute hydrodynamic damping and added mass effects in non-uniform beam by solving unsteady Stokes equation using boundary element techniques.

To develop the methodology for obtaining hydrodynamic forces due to the oscillation of a non-uniform beam (NUB) as shown in Fig. 1, we consider a thin beam with constant and small thickness as compared it its length and width. After describing the parameter associated with a non-uniform beam and its structural mode shape, we briefly present a fluid flow equation based on the unsteady Stokes flow to compute energy dissipation and added mass effects in 2D and 3D flow. Subsequently, we describe BEM procedure to obtain the solution, convergence scheme and discuss its validation. Finally, we validate the model for uniform beam and discuss the influence of non-uniform beams with linearly and quartic varying width on hydrodynamic damping and added mass effect. Subsequently, we extend the procedure to compute the quality factor and added mass effect required for analyzing the performance of resonators. To understand the limitation of the model, we also present finite element based solution using ANSYS and discuss pressure and velocity profiles.

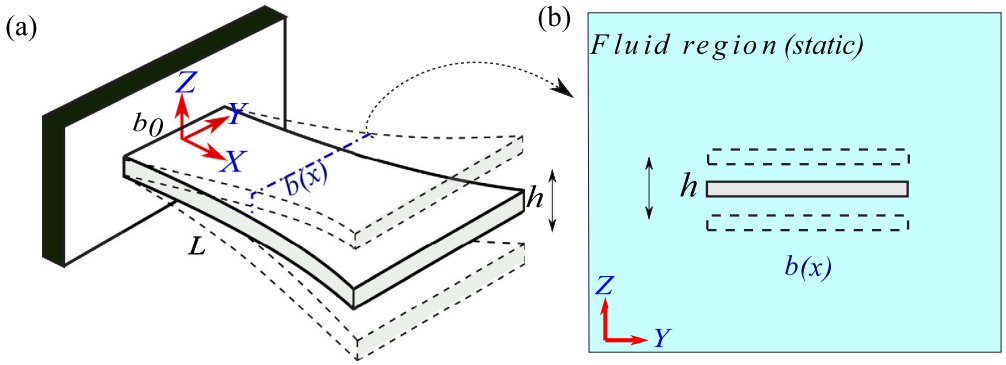

Fig. 1. The non-uniform beam oscillates transversely at first eigen mode in cartesian coordinate system, (a) Schematic representation of a non-uniform cantilever beam with variable width along the length and (b) The sectional view of the non-uniform beam in the static fluid (colored region) in YZ-plane.

2. Mathematical modeling

Consider the non-uniform cantilever beam oscillating in a quiescent incompressible viscous fluid with length L, thickness h, and variable width i.e., $b(x) = b_0(1 + \eta(x/L))^n$ [18,20,67], where b_0 is the fixed end beam width, η represents the tapering parameter (positive and negative values of η denote diverging and converging sections) and n denotes the degree of non-uniform index, i.e., for linear, $n = 1$, and for quartic, $n = 4$, as shown in Fig. 1(a). NUB dimensions are aligned with cartesian coordinates, for example, X-direction is along the length L, Y-direction is along the width $b(x)$, and Z-direction is along the thickness h. The basic assumption of the non-uniform cantilever beam is that the length is substantially more than the width, while the width is much larger than the thickness. However, in the current case, we assumed that thickness is insignificant in order to examine hydrodynamic forces. The cross-section of the beam in the YZ-plane is demonstrated in Fig. 1(b). The boundaries of the fluid domain are considered to be far away from the oscillating structures. The local displacement and velocity around the oscillating non-uniform beam are specified based on the structural modes as described in the next section.

2.1. Structural deformation

To obtain the structural lumped parameters based on the exact modeshape, we consider beam with cross-sectional area $A(x) = b(x)h$, the moment of inertia $I(x) = b(x)h^3/12$, transverse deflection $W(x,t)$ in Z-direction, and the transverse external force $F(x,t)$ including both the hydrodynamic force, $F_h(x,t)$, and the external excitation force, $F_{\text{ext}}(x,t)$. Based on the classical Euler–Bernoulli beam theory [18], the equation of the motion due to bending and its boundary conditions are mentioned in Appendix A and the external transverse force can be written in terms of static external harmonic excitation and hydrodynamic force as $F(x,t) = F_{\text{ext}}(x,t) + F_h(x,t)$. The hydrodynamic force consists of terms proportional to the velocity and acceleration of beam surface, and can be written as $F_h(x,t) = -g_1\partial W(x,t)/\partial t - g_2\partial^2 W(x,t)/\partial t^2$ [1]. Expressing the dynamic response of the beam as $W(x,t) = \phi_i(x)q_i(t)$ and substituting it into Eq. (A.1), we multiply the resultant equation by $\phi_j(x)$ and the integrate it by parts over the length of the beam to obtain the reduced order model as,

$$m_{\text{eff}}\ddot{q}_i + c_{\text{eff}}\dot{q}_i + k_{\text{eff}}q_i = F_{\text{eff}}, \tag{1}$$

where, $m_{\text{eff}} = (m_s(x) + g_2)\int_0^L \phi_i(x)\phi_j(x)dx$, $c_{\text{eff}} = g_1\int_0^L \phi_i(x)\phi_j(x)dx$, $k_{\text{eff}} = \int_0^L EI(x)\phi_i(x)(\partial^4\phi_j(x)/\partial x^4)dx$ and $F_{\text{eff}} = \int_0^L \phi_j(x)F_{\text{ext}}dx$. The g_1 and g_2 are the coefficients which represent effective viscous damping and added mass effect due to the fluid. Consequently, they are proportional to the real and imaginary parts of the complex hydrodynamic force due drag forces [7,8,12].

For the oscillating beam, the transverse deflection can be written as $W(x,t) = \delta\phi_{\text{nu}}(x)e^{i\omega t}$, where δ is the maximum amplitude of oscillation, $\omega = 2\pi/T$ is the angular frequency, T is the time period and ϕ_{nu} is the mode shape or eigenfunction of non-uniform beam in vacuum given by [18,20],

$$\phi^i_{\text{nu}}(x) = A_i\left[\sin\left(\frac{\lambda_i x}{L}\right) - \sinh\left(\frac{\lambda_i x}{L}\right) - \frac{\sin\lambda_i + \sinh\lambda_i}{\cos\lambda_i + \cosh\lambda_i}\left(\cos\left(\frac{\lambda_i x}{L}\right) - \cosh\left(\frac{\lambda_i x}{L}\right)\right)\right], \tag{2}$$

where, A_i is the constant obtained by normalizing the modeshape of cantilever beam such that $\phi_{\text{nu}}(L) = 1$. The corresponding frequency parameters λ_i (i.e., $\omega_i = \left(\frac{\lambda_i}{L}\right)^2\sqrt{\frac{EI}{m_s}}$) and constants A_i for linearly converging and diverging beams are mentioned in Table 1 and those for the quartic converging and diverging beams are mentioned in Table 2. Finally, the transverse velocity along the Z-direction can be written as $\dot{W}(x,t) = i\omega\delta\phi_{\text{nu}}(x)e^{i\omega t}$ which acts as an input to the fluid domain.

2.2. Fluid flow due to oscillating structure

Neglecting gravity and body forces, the flow around the cantilever beam oscillating with small amplitude in an in-compressible and viscous Newtonian fluid can be modeled by the unsteady Stokes equation [47]. Thus, the continuity and linearized momentum equations involving flow variables such as velocity, $\bar{\boldsymbol{u}}(\bar{u}_1(x,y,z,t), \bar{u}_2(x,y,z,t), \bar{u}_3(x,y,z,t))$ and pressure, $p(x,y,z,t)$ [47,62] are mentioned in Appendix B and, taking the boundaries of the thin non-uniform beam as $x \in [0, L]$, $y \in [-b(x)/2, b(x)/2]$ with negligible thickness, the fluid boundary conditions such that the no-slip velocity condition at the fluid-solid interface can be taken. The field variables, velocity, and pressure are also assumed to be zero at infinity. Taking the flow variables $\bar{\boldsymbol{u}} = \boldsymbol{u}e^{i\omega t}$, with $\boldsymbol{u} = [u_1, u_2, u_3]$ and $p = \bar{p}e^{i\omega t}$, where $i = \sqrt{-1}$, ω is the angular excitation frequency, and substituting into Eq. (B.1), we obtain the non-dimensionalized form the equation by normalizing length scale with b_0, velocities with the free stream velocity $V_0 = i\omega\delta$, and pressure with $\mu V_0/b_0$, where, μ is the dynamic viscosity of the fluid. Finally, the non-dimensional formulation of the unsteady Stokes equation can be expressed in the frequency domain as,

$$i\alpha^2 b_0^2\,\boldsymbol{u}(x,y,z,\omega) = -\nabla\bar{p}(x,y,z,\omega) + \nabla^2\boldsymbol{u}(x,y,z,\omega), \tag{3}$$

where, $\alpha^2 = \omega/\nu$, $\nu = \mu/\rho$ is the kinematic viscosity. Finally, to describe the solution for non-uniform beam, we take the non-dimensional cartesian co-ordinate $\xi_1 = x/L$, $\xi_2 = y(x)/b_0 = (1 + \eta\xi_1)^n$ and $\xi_3 = 0$ (negligible thickness) and further discuss the solution based on 3D and 2D flow in the following sections.

2.2.1. 3D flow modeling

To capture the influence of 3D flow on hydrodynamic forces due to oscillation of a thin non-uniform beam, Eq. (3) is solved to obtain the oscillatory stokes velocity in terms of the oscillatory Stokeslet, $\mathcal{G}_{33}$, and stress tensor [38,60,62]. Assuming the negligible beam thickness, the

Table 1
The eigen values λ_i and A^i for linearly converging and diverging beam for the case of $\phi_{nu}(L) = 1$.

η	−0.5	−0.4	−0.3	−0.2	−0.1	0	0.1	0.2	0.3	0.4	0.5
λ_i	2.0765	2.0243	1.9659	1.9357	1.9047	1.8751	1.8474	1.8223	1.7991	1.7782	1.7595
A^i	0.2316	0.2596	0.2893	0.3150	0.3409	0.3671	0.3931	0.4189	0.4447	0.4702	0.4951

Table 2
The eigen values λ_i and A^i for quartic converging and diverging beam for the case of $\phi_{nu}(L) = 1$.

η	−0.5	−0.4	−0.3	−0.2	−0.1	0	0.1	0.2	0.3	0.4	0.5
λ_i	2.7491	2.5095	2.3099	2.1419	1.9984	1.8751	1.7674	1.6730	1.5893	1.5145	1.4477
A^i	0.0849	0.1129	0.1519	0.2047	0.2751	0.3671	0.4856	0.6362	0.8249	1.0587	1.3444

normal direction stress jump is described by $\bar{\sigma}_3 = \bar{p}_3^+ - \bar{p}_3^-$. Compared to the other velocities, only the transverse direction velocity is more dominant. Thus, the non-dimensional form of the transverse velocity vector can be related to the non-dimensional stress jump $\bar{\sigma}^* = \frac{\bar{\sigma}}{\mu V_0/b_0}$. Dropping the asterisk sign, we get,

$$\frac{u_3(\xi_1', \xi_2')}{V_0} = \frac{L}{8\pi} \int_{\xi_1} \int_{\xi_2} \bar{\sigma}_3 \mathcal{G}_{33}(\xi_1, \xi_2, 0; \xi_1', \xi_2', 0|\alpha) d\xi_1 d\xi_2 \tag{4}$$

where, the Stokeslet is defined by,

$$\mathcal{G}_{33}(\xi_1, \xi_2, 0; \xi_1', \xi_2', 0|\alpha) = \frac{1}{L}\left\{ 2e^{\frac{-\sqrt{2\pi i\beta}r'}{\chi}} \left[\frac{1}{r'} + \frac{\chi}{\sqrt{2\pi i\beta} r'^2} - \frac{i\chi^2}{2\pi\beta r'^3} \right] + \frac{i\chi^2}{\pi\beta r'^3} \right\}. \tag{5}$$

Here, $\bar{\sigma}_3(\xi_1, \xi_2)$ represents the stress jump, and $r' = \sqrt{(\xi_1 - \xi_1')^2 + \chi^2(\xi_2 - \xi_2')^2}$ and (ξ_1, ξ_2) are the surface and (ξ_1', ξ_2') are fluid domain points, $\chi = b_0/L$ is the aspect ratio and $\beta = \omega b_0^2/2\pi\nu$ is the frequency parameter, $V_0 = i\delta\omega$ is the maximum velocity amplitude of oscillating structure, δ represents the amplitude of oscillation, $\alpha^2 = \frac{\omega}{\nu} = \frac{2\pi\beta}{b_0^2}$. Since the deflection in the frequency domain is given by $W(\omega) = \delta\phi_{nu}(\xi_1')e^{i\omega t}$, its derivative yields the local velocity in the transverse direction of oscillation as $u_3 = i\delta\omega\phi_{nu}(\xi_1')$. Thus, the velocity ratio on the left side of the Eq. (4) is reduced to $\phi_{nu}(\xi_1')$. Therefore, the boundary integral equation in terms of non-dimensional form can be expressed as,

$$\phi_{nu}(\xi_1') = \frac{L}{8\pi} \int_{\xi_1} \int_{\xi_2} \bar{\sigma}_3(\xi_1, \xi_2, \omega) \mathcal{G}_{33}(\xi_1, \xi_2, 0; \xi_1', \xi_2', 0|\alpha) d\xi_1 d\xi_2. \tag{6}$$

To estimate the unknown stress on the beam surface, we employ the boundary element method. First, the beam is meshed into the required number of unequal panels. Assuming the constant stress jump over the centroid of each panel as initial condition, the above equation is solved by integrating the Greens function using the quad2d package in MATLAB. Moreover, a special care should be taken when fluid and structure points coincide (r' approaching zero), resulting in a numerical singularity. Under this condition, $\mathcal{G}_{33}$ is modified by transforming the cartesian coordinates to polar coordinates $(\xi_1, \xi_2) \to (\rho_\epsilon, \theta)$, where ρ_ϵ is the smaller dimension of the each panel and θ is the angle of rotation $[0, 2\pi]$ [62],

$$\int_{\xi_1} \int_{\xi_2} \mathcal{G}_{33}(\xi_1, \xi_2, 0|\xi_1', \xi_2', 0; \alpha) \mathrm{d}\xi_1 \mathrm{d}\xi_2 = \frac{\chi^2}{4\pi\beta\rho_\epsilon} \left[e^{\frac{-\sqrt{2\pi i\beta}}{\chi}\rho_\epsilon} \left(i - \frac{\sqrt{2\pi i\beta}}{\chi}\rho_\epsilon \right) - i \right]. \tag{7}$$

2.2.2. 2D flow modeling

To compute the hydrodynamic forces using 2D flow, Tuck [47] developed a boundary integral formulation for an oscillating long rigid body with a constant cross section. In this case, Eq. (B.1) is transformed into a vorticity equation by taking curl on both sides which results in the formation of a pressure harmonic equation. Resulting the formation final differential expression in stream function is $\nabla^4\psi = \alpha^2\nabla^2\psi$. The solution of the above equation is obtained by Green function method and detailed analysis is expressed by Tuck [47]. The solution can be modified to include the parameter associated with the thin non-uniform beam of negligible thickness ($\xi_3 = 0$). For the given ξ_1, the stream function at a section of a long thin non-uniform beam can be described in terms of Green functions in non-dimensional form as

$$\psi(\xi_2', \xi_3') = -\int_{-\xi_2}^{\xi_2} \left[\Delta\overline{\omega}(\xi_2, 0) \Psi_{\xi_3}(\xi_2, 0|\xi_2', \xi_3') - \frac{1}{\mu} \Delta\bar{\sigma}_3(\xi_2, 0) \Psi_{\xi_2}(\xi_2, 0|\xi_2', \xi_3') \right] d\xi_2, \tag{8}$$

where, $\Delta\overline{\omega}(\xi_2, 0)$ is vorticity jump and $\Delta\bar{\sigma}_3(\xi_2, 0)$ is pressure or stress jump across the beam at the given section. The Green function $\Psi(\xi_2, 0|\xi_2', \xi_3')$ is represented as

$$\Psi(\xi_2, 0|\xi_2', \xi_3') = -\frac{1}{2\pi\alpha^2} \left[\log(\alpha \mathrm{R}) + \mathrm{K}_0(\alpha \mathrm{R}) \right], \tag{9}$$

where, $\mathrm{R} = \sqrt{(\xi_2 - \xi_2')^2 + (\xi_3')^2}$. and K_0 denotes the Bessel function of the third kind with zero order. The lateral and transverse velocities on the beam section are calculated by taking the $u_2 = \psi_{\xi_3}(\xi_2', \xi_3')$ and $u_3 = -\psi_{\xi_2}(\xi_2', \xi_3')$, respectively. By considering the $\xi_3' = 0$ on the beam along the width, the transverse velocity is directly relate with the pressure jump $\Delta\bar{\sigma}_3(\xi_2, 0)$ but no vorticity jump across the beam because the first term of the Eq. (8) i.e., $\Psi_{\xi_3}(\xi_2, 0|\xi_2', 0) = 0$, with $R = (\xi_2 - \xi_2')$. The lateral velocity is gives the vorticity jump but having a continuous pressure.

Subsequently, we require to consider the transverse velocity of the beam across the beam by differentiating Eq. (8) with ξ_2' i.e., $u_3 = -\psi_{\xi_2}(\xi_2', 0)$ at a given section of the beam ξ_1. Finally, we obtained a transverse velocity of the beam in non-dimensional form is

$$\phi_{nu}(\xi_1) = \int_{-\xi_2}^{\xi_2} \bar{\sigma}_3(\xi_2, 0) \Psi_{\xi_2\xi_2'}(\xi_2, 0|\xi_2', 0) d\xi_2'. \tag{10}$$

Initial pressure jump is considered as constant over unequal number of segments at a given ξ_1 in order to perform integration over a segment using BEM [8,47]. Subsequently, the complex BEM square matrix is obtained and inverted to obtain the pressure jump of the beam at particular section at ξ_1. In the subsequent section, we describe the computation of hydrodynamic functions using the complex stress jump obtained for 2D and 3D flow. Later, we compare the solution based on 3D and 2D flow using Eqs. (6) and (10) discuss the limitation of 2D solution.

2.3. Evaluation of force and hydrodynamic function

To find the non-dimensional forces in the frequency domain on non-uniform cantilever beam surface, the non-dimensional stress jump obtained previously are integrated over the defined non-uniform surface in terms of Riemann summation as,

$$\bar{F}(\omega) = \mu V_0 L \int_{\xi_1} \int_{\xi_2} \bar{\sigma}_3(\xi_1, \xi_2) d\xi_1 d\xi_2. \tag{11}$$

Using the hydrodynamic function Γ_x obtained for a rigid circular cylinder [25,47], we obtain the average hydrodynamic force by performing integration over the length of the beam in terms of average hydrodynamic function $\bar{\Gamma}$ as,

$$\bar{F}(\omega) = \frac{\pi}{4} \rho\omega b_0^2 V_0 L \bar{\Gamma}(\beta, \eta, \chi) = \mathrm{Re}(\bar{F}) + i\mathrm{Im}(\bar{F}). \tag{12}$$

Using $V_0 = i\delta\omega$ and complex form of hydrodynamic function, total force can be separated into real and imaginary components. While, the real component of hydrodynamic force represents damping force and imaginary component gives the thrust force. Whereas, the average and local hydrodynamic function can be written as,

$$\bar{\Gamma}(\beta,\eta,\chi) = \frac{2}{\pi^2\beta}\int_{\xi_1}\int_{\xi_2}\bar{\sigma}_3(\xi_1,\xi_2)d\xi_1 d\xi_2 \tag{13}$$

and

$$\Gamma_x(\beta,\eta,\chi) = \frac{2}{\pi^2\beta\phi_{nu}}\int_{\xi_2}\bar{\sigma}_3(\xi_1,\xi_2)d\xi_2, \tag{14}$$

in terms of frequency parameter β, tapering parameter η, aspect ratio χ, and non-uniform index n. Here, the real and imaginary components of the complex-valued hydrodynamic function are related with the thrust force and dissipation. Finally, the virtual added mass and damping coefficient are obtained from the thrust force and energy dissipation to find the corresponding damping ratio and frequency shift.

2.3.1. Energy loss (ΔE)

To find the average energy dissipation per cycle with time period $(2\pi/\omega)$, the total damping force is multiplied by the velocity of the beam corresponding to its modeshape and integrated over one cycle as [1,62],

$$\Delta E = \int_0^{2\pi/\omega}\bar{F}(\omega)\omega\delta\phi_{\mathrm{nu}}(\xi_1)\sin\omega t dt. \tag{15}$$

Alternatively, it can be written as

$$\begin{aligned}\Delta E &= 2\mu\delta^2\omega L\,\mathrm{Re}\left[\int_{\xi_1}\int_{\xi_2}\bar{\sigma}_3\phi_{\mathrm{nu}}(\xi_1)d\xi_1 d\xi_2\right]\\ &= \frac{4\pi\mu^2\delta^2}{\rho b_0}\frac{\beta}{\chi}\,\mathrm{Re}\left[\int_{\xi_1}\int_{\xi_2}\bar{\sigma}_3\phi_{\mathrm{nu}}(\xi_1)d\xi_1 d\xi_2\right].\end{aligned} \tag{16}$$

The total energy of the beam can be computed from the maximum kinetic energy in vacuum. Using the maximum velocity $V_{max} = i\delta\omega(\phi_{\mathrm{nu}})_{\max}$ based on the maximum amplitude corresponding to the mode shape of non-uniform beam, the total energy can be obtained from,

$$E = \frac{1}{2}\rho_b b_0 hL\int_{\xi_1}(1+\eta(x/L))^n V_{\max}^2 d\xi_1. \tag{17}$$

Finally, the damping ratio is obtained from,

$$\zeta = \frac{1}{4\pi}\frac{\Delta E}{E} = \frac{\rho b_0}{2\pi^2\beta\rho_b h}\frac{\int_{\xi_1}\int_{\xi_2}\bar{\sigma}_3\phi_{nu}(\xi_1)d\xi_1 d\xi_2}{\int_{\xi_1}(1+\eta(x/L))^n(\phi_{\mathrm{nu}})_{\max}^2 d\xi_1} \tag{18}$$

and the quality factor is calculated using $Q = 1/2\zeta$.

2.3.2. Hydrodynamic mean thrust ($\mathcal{T}_h$)

To capture the influence of added mass effect, the hydrodynamic thrust force can be found from the total hydrodynamic force. Using $Re_l = \rho\delta\omega L/\mu$ and its ratio with β, $Re_l/\beta = 2\pi\delta/(\chi^2 L)$, the thrust force corresponding to the virtual mass $((\pi/4)\rho b_0^2)$ of a uniform beam with rigid motion can be found from either $0.1963\mu^2\chi^2 Re_l^2\rho^{-1}$ [64], and $0.037\mu^2\chi^2 Re_l^2\rho^{-1}$ [19], respectively. However, for non-uniform beam, the hydrodynamic mean thrust force can be calculated by averaging the product of the stress jump and normal vector $(d\phi/dx)$ over a cycle. Thus, the above expression given by Lighthill [64] can be modified for the non-uniform beam as $0.1963\mu^2\chi^2 Re_l^2\rho^{-1}(1+\eta\xi_1)^{2n}$ for the rigid motion.

To include the effect of flexural mode of non-uniform beam, we find the mean hydrodynamic thrust using imaginary component of hydrodynamic force in non-dimensional form as

$$\mathcal{T}_h = \mathrm{Im}\left[\frac{1}{2\pi^2\beta}\int_{\xi_1}\int_{\xi_2}\bar{\sigma}_3\frac{d\phi}{d\xi_1}d\xi_1 d\xi_2\right]\frac{\mu^2}{\rho}Re_l^2\chi^2 = \mathcal{K}\frac{\mu^2}{\rho}Re_l^2\chi^2. \tag{19}$$

Subsequently, the virtual added mass is found by comparing it with the maximum kinetic energy. Computing the virtual mass incremental factor Λ [73] as the ratio of the virtual mass based kinetic energy to the maximum kinetic energy of beam, we get,

$$\Lambda = \mathrm{Im}\left[\frac{2}{\pi\beta}\frac{\int_{\xi_1}\int_{\xi_2}\bar{\sigma}_3\phi d\xi_1 d\xi_2}{\int_{\xi_1}(1+\eta\xi_1)^{2n}\phi_{max}^2 d\xi_1}\right]\frac{\rho b_0}{\rho_b h} = \Pi(\rho b_0/\rho_b h). \tag{20}$$

Using the virtual mass incremental factor, we obtain the ratio of the frequency of beam in fluid to the frequency of beam in vacuum as,

$$\frac{\omega_f}{\omega_v} = \frac{1}{\sqrt{1+\Lambda}}. \tag{21}$$

3. Boundary element method

In this paper, the boundary element method (BEM) is used to solve the boundary integral equation for a given domain. In the present case, the domain of integration is specified as $D \in [(0,L)\times(-b(x)/2, b(x)/2)\times t, t\approx 0]$. The beam is defined as a mathematical surface with zero thickness. Eq. (4) is solved using the BEM approach to evaluate integration by discretizing the surface into small sections. It is to be noted that the mathematical surface of non-uniform beam (NUB) is discretized into the unequal segments using trigonometric refinement towards the edges. [8,47,62]. As a result, the finer mesh develops near the edges, while the coarser mesh forms closer to the center of the NUB surface. Thus, the panels of NUB are non-rectangular quadrilateral in shape as shown in Fig. 2(b)–(e), while panels of uniform beam are perfectly rectangular illustrated in Fig. 2(a).

To solve the boundary integral equation given by Eq. (6), both structural and fluid points are defined by (ξ_1,ξ_2) and (ξ_1',ξ_2'), respectively, as shown in Figs. 2(a)–(e) in 3D flow. For non-uniform beams, the position of nodes may change for a given tapering parameter η and a tapering index n. The surface and fluid points represent the mesh node and panel centroid, respectively. The centroid of each panel is computed using inbuilt functions "polyshape" to create polygon and "centroid" to find centroid of associated polygon in MATLAB. The mesh and centroid points of each panel of NUB are schematically shown in Fig. 2(a)–(e) for the extreme case of the tapering parameters (η) and with a tapering index n for linear and quartic varying beams. The stress jump on each panel is assumed to be constant. The "quad2d" in MATLAB is used to perform the double numerical integration on each panel by employing the lower and upper bound of limits in the (ξ_1,ξ_2) direction. The tapering parameter η and tapering index n are involved in the limit bound of the ξ_2 direction to capture the influence of non-uniform beam. For the given parameters β,η,n, and χ (aspect ratio), numerical integration is conducted on each panel to generate a complex BEM matrix [7,8,36,38,62]. Considering the number of panels in ξ_1 direction as M and that in ξ_2 direction as N, the total number of panels is given by $M\times N$. For each fluid panel, we obtain the BEM matrix of size $M\times N$. Since, we have $M\times N$ fluid panels, we obtain the final complex global BEM matrix with a dominant diagonal term of size $M^2\times N^2$. The resultant BEM matrix is completely inverted once to evaluate the $\bar{\sigma}_3$ with the no-slip and transverse velocity condition applied to Eq. (6). To determine the stress jump over the non-uniform mathematical surface, the same approach can be applied to NUB with different tapering parameters.

Similarly, the BEM procedure for the long and thin beam using 2D flow can be described in YZ-coordinate system for a given width of $b(x)$ at a specific location of X. In the non-dimensional coordinate system, the thin beam is discretized with unequal segments (i.e., M) by trigonometric refinement as shown in Figs. 3. It helps to eliminate the square root singularities of pressure jump at the extreme node of the beam [47]. The pressure jump assumed to be constant over the beam segment and is located at the center point of the segment. The segment nodes treated as the beam points and mid point of it represent as fluid points. For a given fluid point, the integration of Eq. (10) is performed using the all beam points resulting in the formation of the complex square BEM matrix of size $M\times M$. The diagonal terms of the BEM matrix

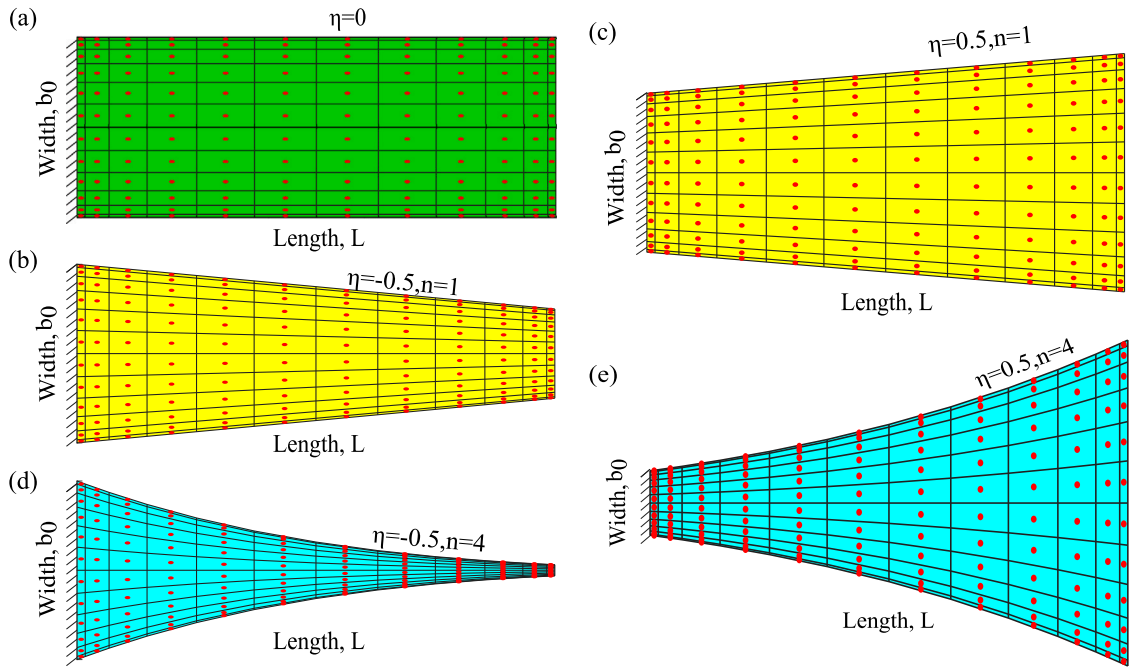

Fig. 2. The trigonometric refinement of the mesh near the edges, the mesh (black lines) and centroid points (red dots) of a each panel for a aspect ratio $\chi = 1/10$ and 12×12 mesh size for all type of beams (a) uniform beam (green color) (b) linearly converging beam (yellow color) (c) linearly diverging beam (yellow color) (d) quartic converging beam (cyan color) (e) quartic diverging beam (cyan color).

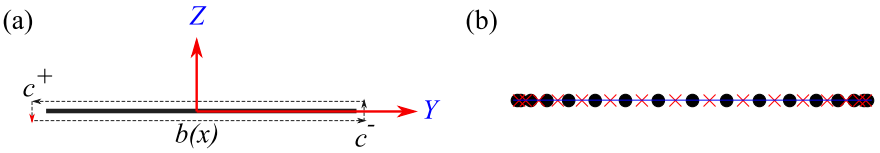

Fig. 3. The 2D thin beam with a variable width in YZ-coordinate system (a) represent contour of integration of the thin beam and (b) represents the unequal spacing of nodes (black dot) and mid points of segments (red cross).

are dominate than the off-diagonal terms. Inverting the BEM matrix by considering the no-slip velocity condition, pressure jump vector of size $M \times 1$ is obtained. Subsequently, the pressure jump is used for the computation of hydrodynamic drag forces and hydrodynamic function.

3.1. Mesh convergence

Since, the width of non-uniform beams vary for different tapering parameters, it is required to perform mesh convergence study to fix number of panels in 3D flow and segment in 2D flow problem. To determine the force acting on the beam using the non-dimensional stress jump, it is necessary to double integrate the stress jump across the non-dimensional surface in the coordinate system (ξ_1, ξ_2). The sum of the contribution of each term is being used to evaluate all integration calculations. The percentage error of the average real and imaginary average forces per $\mu\omega\delta L$ (i.e., non-dimensional total hydrodynamic force) acting on the NUB is illustrated in Fig. 4 at frequency parameter $\beta = 1000$ and aspect ratio $\chi = 1/10$. It is clear that the mesh distribution along the width varies in each cases of NUB. Furthermore, we maintain a consistent mesh distribution for the uniform beam. For UB (uniform beam), LCB (linearly converging beam), LDB (linearly diverging beam), QCB (quartic converging beam), and QDB (quartic diverging beam), the mesh size is varied from 64 to 4.096×10^3, 0.512×10^3 to 3.072×10^3, 64 to 5.12×10^3, 1.204×10^3 to 2.304×10^3, and 2.048×10^3 to 6.144×10^3, respectively. In each case, the percentage errors of real and imaginary parts of the non-dimensional total hydrodynamic average forces acting on each beam extreme tapering parameters, i.e., $\eta = -0.5$ and 0.5 for both linear and quartic tapering index are illustrated in Fig. 4(a). The higher mesh represents the converged non-dimensional total hydrodynamic force under which the percentage error is less than 5% for both real and imaginary non-dimensional forces $\bar{F}$. The real and imaginary stress jump contours on the quartic converging ($\eta = -0.4$) and diverging ($\eta = -0.4$) beams at $\beta = 1000$ and $\chi = 1/10$ are shown in Fig. 4(b) and (c), respectively.

3.2. Validation

To compare the drag force from the present model, we take the quality factor for the linearly varying non-uniform and uniform beams obtained from experiments as presented by Ashok. et al. [54,67]. Appropriate parameters of silicon dioxide non-uniform beams such as the width at fixed end $b_0 = 40$ μm, thickness, $h = 0.95$ μm, and its length $L = 200$ μm with aspect ratio of $\chi = 1/5$, and its density $\rho_b = 2200$ kg/m^3 are taken from [18,54,67]. The density and the viscosity of the fluid are $\rho = 1.2$ kg/m^3, and $\mu = 1.8 \times 10^{-5}$ Pa-s, respectively. Using the measured frequencies of linearly varying non-uniform beam [67], the frequency parameter is obtained for tapering parameter varying from −0.6 and 0.6 as mentioned in Table 3. As the resonance frequency decreases from converging to diverging beam, the frequency parameter β also reduces. The quality factor increases as tapering parameter varies from −0.6 and 0.6 as described by Q_f computed using the present method. The same trend is observed in the experimental studies except for the last case of 0.6 possibly due to the influence of bottom substrate which is not considered in the present study. On comparing the quality factor, we found except for extreme cases, theoretical quality factor is with-in 10% of percentage

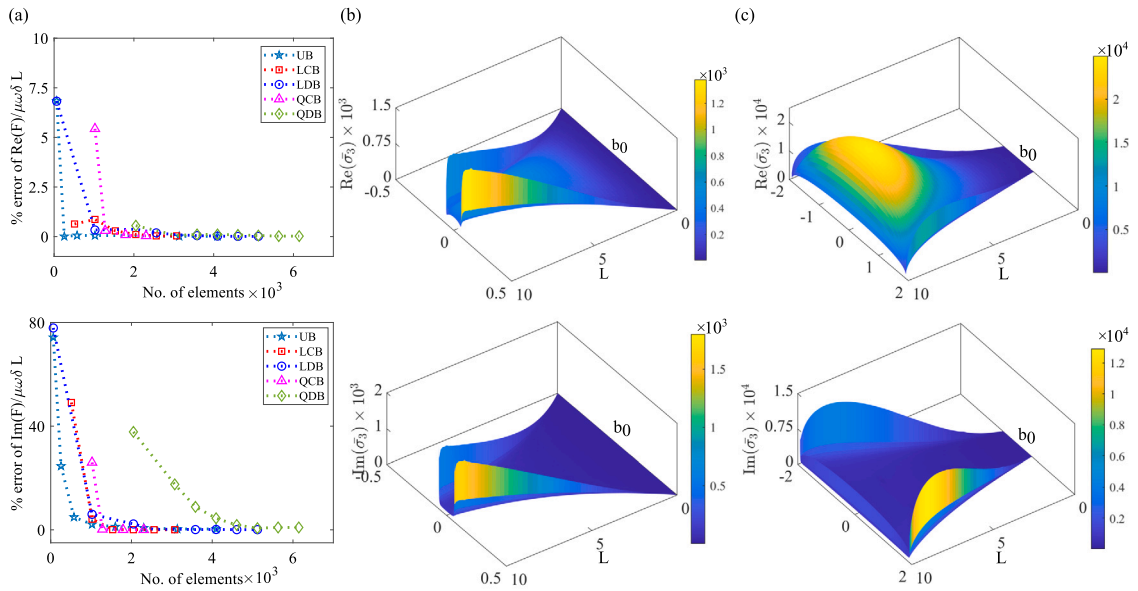

Fig. 4. The convergence study is performed at $\beta = 1000$, $\chi = 1/10$ and all extreme tapering parameter at ($\eta = -0.5, 0.5$) for linear and quartic converging-diverging beam i.e., UB, LCB, LDB, QCB and QDB. The require number of mesh size is different for each case. Representation of % error of (a) real and imaginary average force on the NUB, (b) real and imaginary part of the stress jump on the quartic converging beam (QCB) at $\eta = -0.4$, (c) real and imaginary part of the stress jump on the quadratic diverging beam (QDB) at $\eta = 0.4$.

Table 3
The comparison of the quality factor with the experiment at given resonance frequency for a linearly converging and diverging variation.

η	f(kHz) [67]	β	Q_f (Present)	Q_f [54,67]	%error
−0.6	27.7999	2.9653	28.1847	24.0594	17.14
−0.4	24.4495	2.6080	29.2647	27.0490	8.19
−0.2	21.9331	2.3395	30.5747	31.1005	1.69
0	21.18	2.2592	32.3171	30.0000	7.72
0.2	19.5667	2.0871	33.5424	36.9040	9.10
0.4	18.7163	1.9964	35.002	41.9571	16.57
0.6	17.6999	1.8880	38.0139	32.927	15.44

error. The deviation from experiments are due to measurement error and other structural damping losses [67]. In the subsequent section, we restrict our studies to analyze the influence of tapering parameter on the hydrodynamic forces of non-uniform beam to its first bending mode using 3D and 2D flow condition.

4. Results and discussions

To investigate the variation of the total hydrodynamic function of a three-dimensional NUB for linearly and quartic converging and diverging beams, we perform non-dimensional analysis over the frequency parameters $\beta \in [1, 1000]$. The computation of the local hydrodynamic function is based on the exact mode shape of the beam as a function of tapering parameter to account for linear and quartic variation of NUB. To compute accurate values of hydrodynamic forces in non-uniform beam, either 3D or 2D flow models can be used. To know the limitation of 2D flow model under the long beam assumption, results from both the models are compared as a function of aspect ratios. Subsequently, the variation of hydrodynamic forces are done as a function of frequency parameter for different NUBs. Finally, damping and added mass effects are found and compared for different aspect ratios of non-uniform beam with varying tapering parameter.

4.1. Linear converging and diverging beams

To compare the real and imaginary hydrodynamic functions due to the vibration of linear non-uniform beam in its first bending mode obtained using 3D and 2D flow model, the aspect ratio of the beam is varying from 0.05 to 1, i.e., $\chi \in [0.05, 1]$. The lower value represents extremely long beam and unity represents the square beam. Here, the real and imaginary components of hydrodynamic functions also represent added mass and damping effects. Since real and imaginary components of hydrodynamic functions are function of frequency parameter β and χ, we compute these functions at mid-section (x = L/2) corresponding to a fixed $\beta = 1000$ for comparing their values for uniform beam (UB), linearly converging beam (LCB) with $\eta = -0.5$, linearly diverging beam (LDB) with $\eta = 0.5$ as shown in Fig. 5.

Fig. 5(a) and (d) illustrate the variations of hydrodynamic functions of UB with aspect ratio. It shows that the value computed using 3D flow is closer to that from 2D flow with error of less than 1% for the long beam with aspect ratio less than 0.25. For $\chi = 1$, the percentage difference between real and imaginary components are nearly 22% and 18%, respectively. Therefore, 2D flow model for long thin beam can be used till the aspect is below 0.25. Similarly, observing the variation of these quantities for LCB and LDB in Figs. 5(b)–(f), we found that the results based on 3D flow model deviates from 2D flow beyond $\chi = 0.2$. Moreover, the percentage deviation of the real and imaginary components of LCB at $\chi = 1$ are found to be 20% and 16%, if 2D flow model is used. For LDB, the percentage errors are found to be 43% and 27%. Thus, it is concluded that if 2D model is used in computing the hydrodynamic forces, percentage errors may vary from minimum of 16% to maximum of 43%. At lower values of aspect ratios, we found that all the models converge to the same values. However, the real hydrodynamic function is lowered by 42% for LCB and increased by 52% for LDB with respect to that of uniform beam with $\chi < 0.2$ at $\beta = 1000$. The corresponding imaginary components of LCB and LDB deviate by 26% with respect to that of uniform beam. The hydrodynamic coefficients deviate more with respect to the 2D results at $\chi = 1$ due to the presence of non-trivial pressure gradients along the length as well as the width.

To know the influence of frequency on the added mass and damping effects, we compare the real and imaginary components of hydrodynamic function using 3D and 2D flow model for a long thin beam of aspect ratio, $\chi = 0.1$ by varying β from 1 to 1000. Fig. 6(a) and (c) show

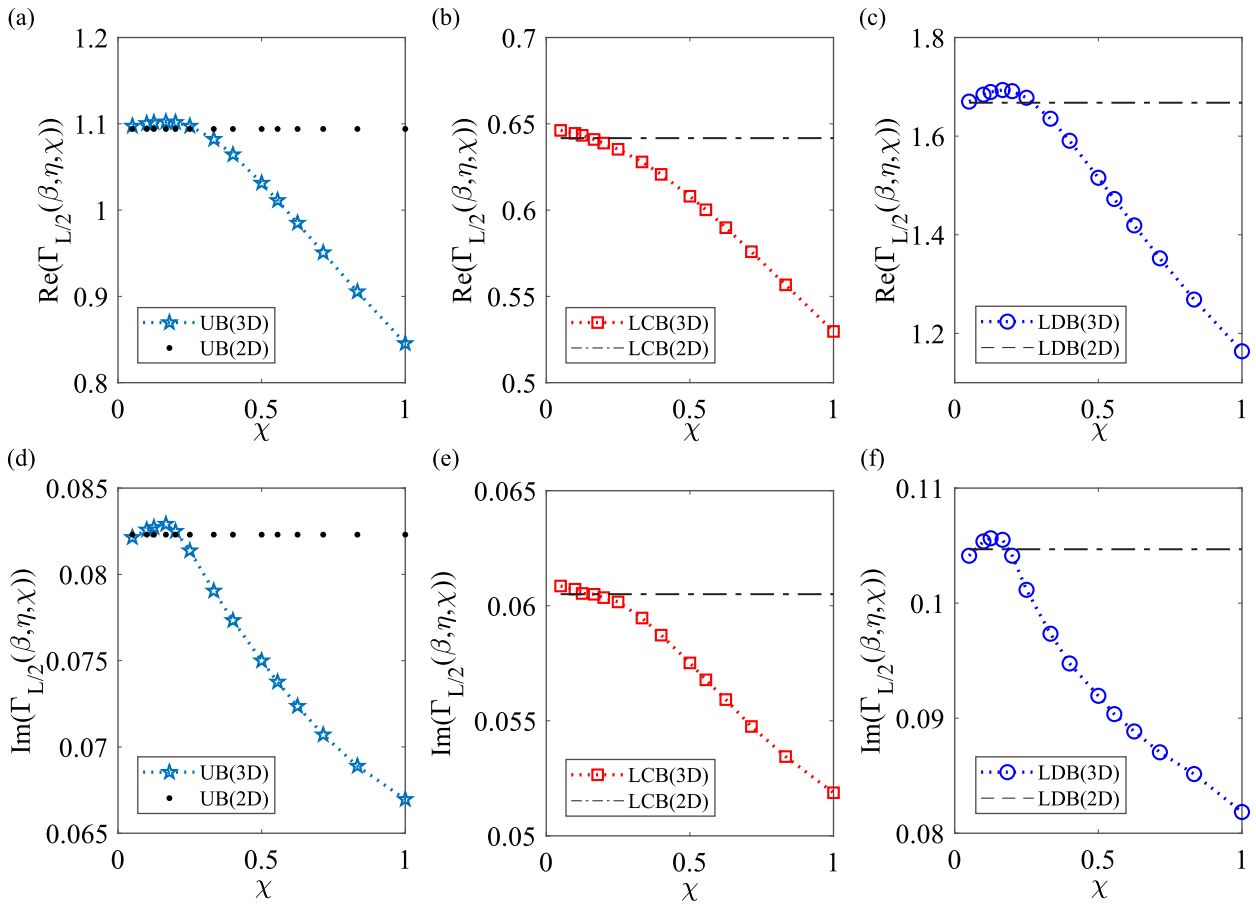

Fig. 5. Linear hydrodynamic function is varying with the increasing aspect ratio from 0.05 to 1. The comparison of three dimensional non-uniform beam hydrodynamic function at $\beta = 1000$ at mid location of the NUB with long TBT (2D) with black different lines under consideration of tapering parameter. Plots (a), (b) and (c) denotes the added mass coefficient, and (d), (e) and (f) damping coefficient for UB($\eta = 0$,star), LCB($\eta = -0.5$,square), and LDB ($\eta = 0.5$,circle).

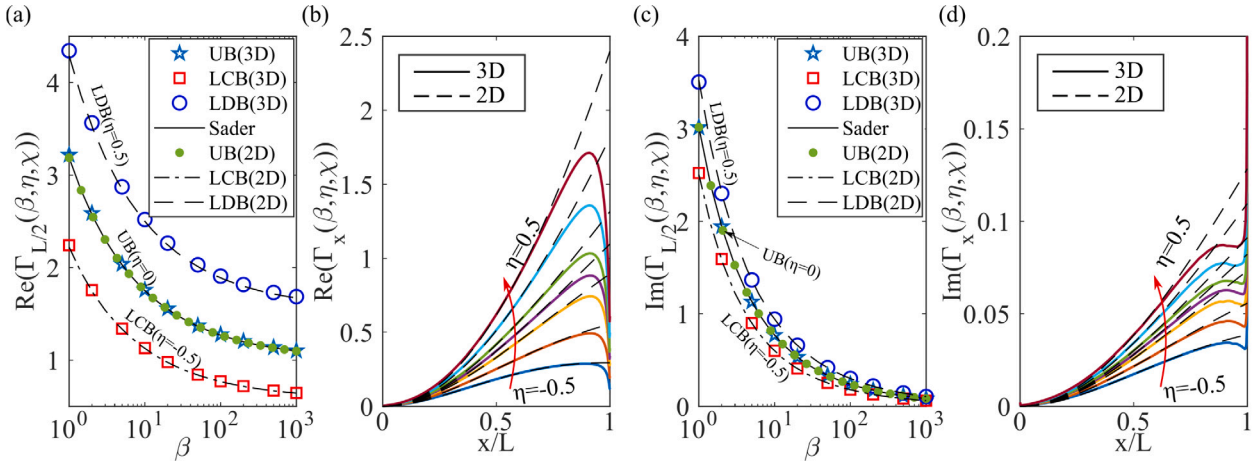

Fig. 6. The variation of linear hydrodynamic function is with respect to the frequency parameter β and along the non-dimensional length of the beam $\xi_1 = x/L$, (a) represents the real part of the hydrodynamic function in 3D (colored shaped marker) and 2D (black solid/dashed lines) w.r.t., β at the mid location of the beam while it is in rigid oscillation at $\chi = 1/10$, (b) denotes the real part of $\Gamma_x(\beta, \eta, \chi)$ along the length of the beam at exact modeshape of NUB at $\chi = 1/10$ and $\beta = 1000$ with increasing tapering parameter η, −0.5 (LCB) to 0.5 (LDB) of a 3D (solid colored lines) and 2D (dashed black lines), (c) represents the imaginary part of the hydrodynamic function in 3D (colored shaped marker) and 2D (black solid/dashed lines) w.r.t., β at the mid location of the beam while it is in rigid oscillation at $\chi = 1/10$, (d) denotes the imaginary part of $\Gamma_x(\beta, \eta, \chi)$ along the length of the beam at exact modeshape of NUB at $\chi = 1/10$ and $\beta = 1000$ with increasing tapering parameter η, −0.5 (LCB) to 0.5 (LDB) of a 3D (solid colored lines) and 2D (dashed black lines).

variation of the hydrodynamic functions computed at $x = L/2$ of the oscillating uniform and non-uniform beams with tapering parameter 0.5 and −0.5. The results for uniform beam are also compared with the 2D model obtained by Sader [12]. It is interesting to note that all the models show the same decreasing values at different values of β for long and thin beam with $\chi = 0.1$. Also, the hydrodynamic coefficients for converging beams are more and that for diverging beams are less as compared to that of uniform beam.

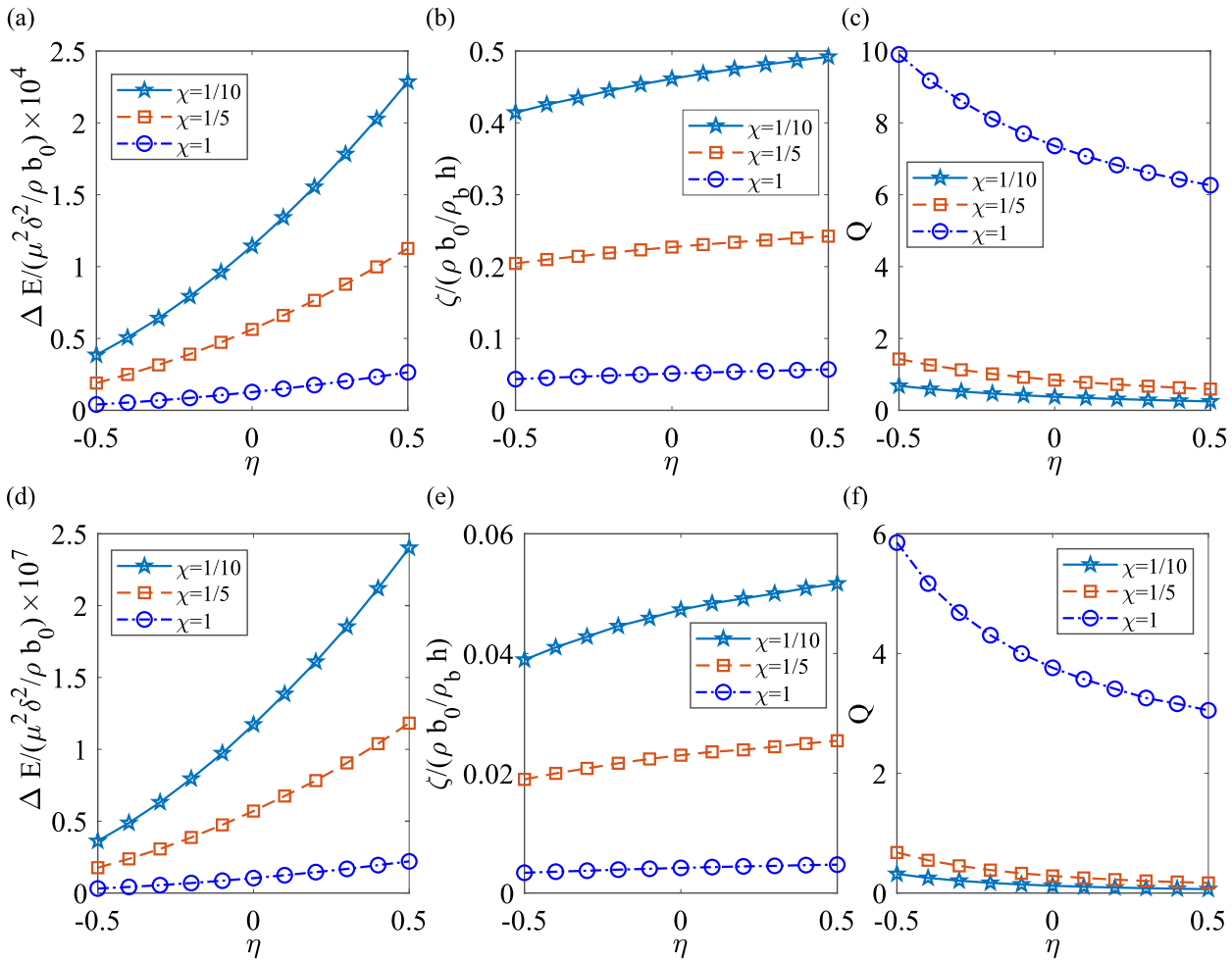

Fig. 7. The effect of the tapering parameter of linearly converging and diverging beam (−0.5 to 0.5) on the energy loss ΔE, damping ratio ζ and quality factor Q. The plots (a), (b), and (c) are the energy loss, damping ratio, and quality factor at $\beta = 10$ at various aspect ratios, i.e., $\chi = 0.1, 0.2, 1$, respectively. And the plots (d), (e), and (f) are the energy loss, damping ratio, and quality factor at $\beta = 1000$ at various aspect ratios, i.e., $\chi = 0.1, 0.2, 1$, respectively.

The real hydrodynamic function values of LDB, LCB and UB vary from 4.34 to 1.68, 2.24 to 0.64, and 3.22 to 1.10, respectively, when β varied from 1 to 1000. Thus, at $\beta = 1$, the values are increased by 36% in case of LDB and reduced by 30% in case of LCB with respect that of UB. Similarly, at $\beta = 1000$, real component in case of LDB is increased by 51.5% and that in LCB is decreased by 46.23% w.r.t to the values of UB. The corresponding imaginary components of hydrodynamic functions of LDB, UB, and LCB vary from 3.53 to 0.11, 3.02 to 0.09, and 2.52 to 0.06, respectively, due to change in β over the same range of 1 to 1000. Thus, the similar trends are observed in the imaginary components in which 17% and 28% differences are observed for LDB, and 16% and 26% differences are observed for LCB at $\beta = 1$ and 1000, respectively. Therefore, the real and imaginary parts of the hydrodynamic function reduce with increase in β as the unsteady boundary layer becomes small and vortex is generated due to the non-linear convective force at larger β.

To investigate the difference of results between 3D and 2D flow model, we also computed hydrodynamic functions at different locations of the long beam with $\chi = 0.1$ for a given $\beta = 1000$ as shown in Fig. 6(b) and (d). It shows that hydrodynamic effect increases along the length of the beam. However, further analysis indicate that 2D flow model deviates from 3D flow model at $x/L = 0.7$ for the tapering parameter 0.5. This deviation point shifts towards the free end with decrease in tapering parameter. Since, at the trailing edge the oscillation amplitude is maximum, the maximum value of the hydrodynamic function shifts towards the free end which is clearly observed in 2D as well as 3D models. As the damping and added mass coefficients explicitly influence the energy loss [1,62] and thrust production [49,64], respectively, we discuss their variation in detail in the following subsection. .

4.1.1. Energy loss, damping ratio and quality factor

Due to the hydrodynamic damping on the linearly converging and diverging beam, the energy loss is evaluated on the surface of the beam from Eq. (16). The energy loss $\Delta E/(\mu^2\delta^2/\rho b_0)$ on the beam is explicitly dependent on the velocity and stress jump on the beam. Fig. 7(a) and (d) show the variation of energy loss versus tapering ratio of NUB for $\beta = 10$ and $\beta = 1000$, respectively. Considering the various aspect ratio, χ, the energy loss gradually increases as the tapering parameter increases from −0.5 to 0.5. For long beam with $\chi = 0.1$, the losses are found to be more as compared to those for $\chi = 0.2$ and $\chi = 1$. It is observed that as β increased from 10 to 1000, the magnitude of energy loss also increased by 3 order of magnitude. It is due that fact the energy loss given by Eq. (16) is proportional frequency parameter β. Figs. 7(b) and (e) show the variation of damping ratio for the unit $(\rho b_0/\rho_b h)$ of the beam and fluid. As in the case of energy loss, the damping ratio factor gradually increases with the tapering parameter, and its magnitude is more for a smaller aspect ratio for the corresponding frequency parameter. The surface area of the linearly diverging beam has cooperatively more than the linearly converging beam. Furthermore, the contact area of the fluid to the surface is more at the linearly diverging beam, and it creates more energy loss

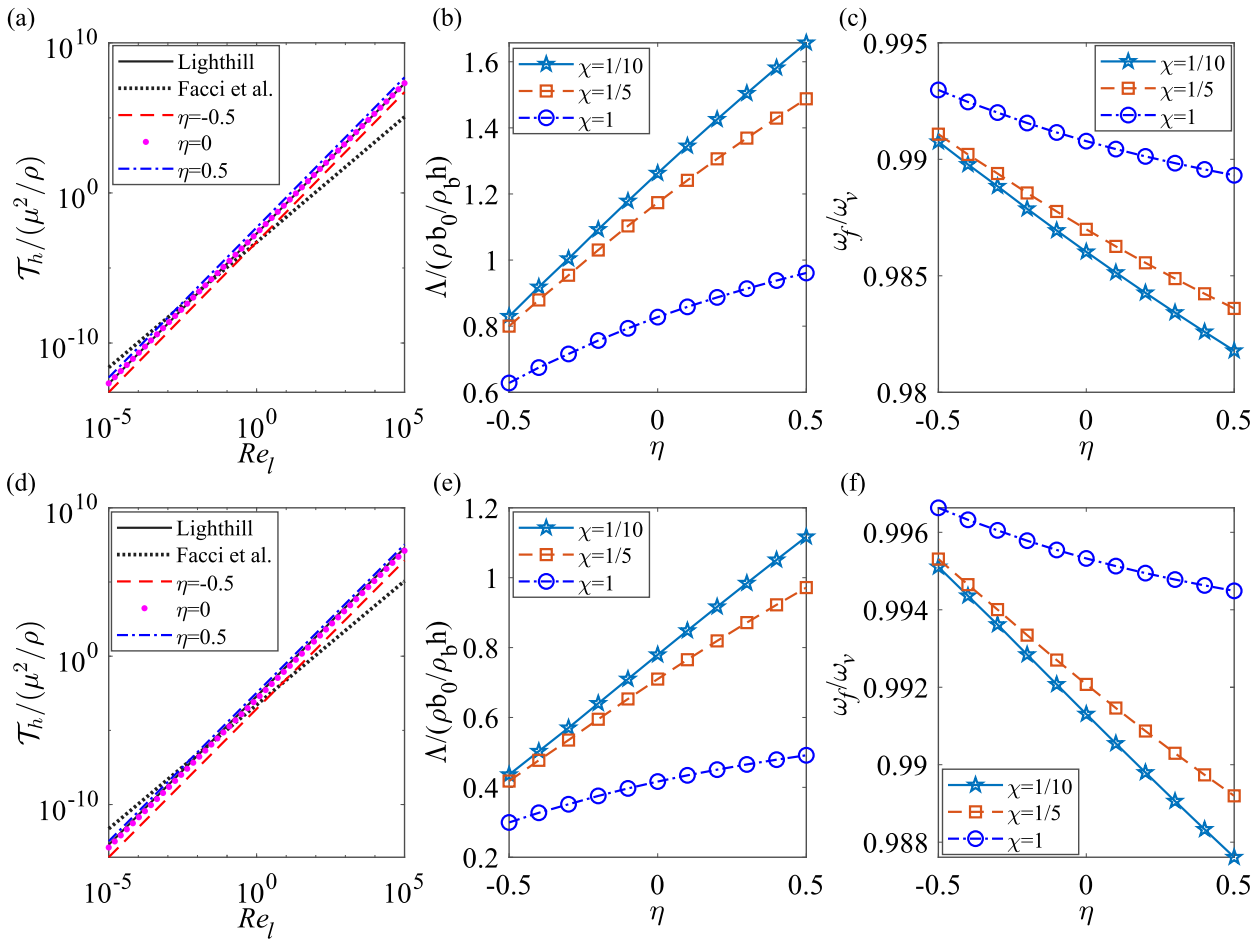

Fig. 8. The linear hydrodynamic thrust force ratio on the NUB at extreme tapering parameter i.e., $\eta = -0.5, 0, 0.5$ with respect to the Re_l for a $\chi = 1/10$, (a), and (d) represents at $\beta = 10$, and 1000, respectively. The virtual added mass factor Λ of the beam with varying the tapering parameter η from −0.5 to 0.5 (b), and (e) are representing the Λ at $\beta = 10$, and 1000 at various aspect ratio $\chi = 0.1, 0.2\&1$, respectively. Plots (c) and (f) represents the frequency ratio at $\beta = 10$ and 1000 for various η from −0.5 to 0.5 at various aspect ratio $\chi = 0.1, 0.2\&1$.

as compared to the beam with a lower aspect ratio. Increasing the aspect ratio to one, the magnitude of the damping ratio factor decreases further. It is also found that damping ratio is more for lower values of $\beta = 10$ as compare to that for higher value $\beta = 1000$. It is due to the fact that the damping ratio is inversely proportional to frequency parameter. Fig. 7(c), and (f) represent the quality factor computed from the damping ratio using the appropriate properties of fluid and beam at $\beta = 10$, and $\beta = 1000$. In both the cases the Quality factor is high for linearly converging beam with $\eta = -0.5$ and low for linearly diverging beam with $\eta = 0.5$. Additionally, it is more, beam with aspect ratio of 1 and lowest for beam with aspect ratio of 0.1. Thus, it is found that quality factor of converging beams are more as compared to diverging beam.

4.1.2. Hydrodynamic mean thrust and virtual added mass factor

To investigate the influence of added mass effect of fluid on the structure, we compute the mean thrust force capturing inertial effects of small volumes of fluid surrounding the vibrating NUB called as virtual mass. The thrust force which is acting perpendicular to its mid axis of the oscillating structure with a small amplitude is estimated from the rate of momentum change between the non-uniform beam (NUB) and the fluid over a given cycle. The hydrodynamic mean thrust can be computed from Eq. (19) which is mainly dependent on the Re_L and aspect ratio χ. It also noticed that the theoretical [64] and numerical [19] estimation of the mean thrust involves the computation of only the coefficients such as $\mathcal{K}$ in Eq. (19). In this paper, this coefficient $\mathcal{K}$ is evaluated by the BEM approach using the imaginary part of the stress jump and normal vector on the NUB surface at specific frequency parameter β, tapering parameter η and aspect ratio χ. At $\beta = 10$ and $\chi = 0.1$, $\mathcal{K}$ values are found as 0.052, 0.20 and 0.50, respectively, for the NUB with various tapering parameters, i.e., −0.5, 0 and 0.5. At higher frequency with parameters $\beta = 1000$ and $\chi = 0.1$, the coefficient $\mathcal{K}$ of the LCB ($\eta = -0.5$), UB($\eta = 0$) and LDB($\eta = -0.5$) are obtained as 0.028, 0.13 and 0.34. It is found that $\mathcal{K}$ for uniform beam closely matched with that given by Lighthill [64].

Subsequently, we compute the $\mathcal{K}$ coefficients for the calculation of mean thrust per μ^2/ρ on the NUB at $\beta = 10$ and 1000 when Re_L varies from 10^{-5} to 10^5 at $\chi = 0.1$ as shown in Figs. 12(a) and (d). The computed thrust is found to be in agreement with the theoretical values with percentage error of less than 2%. The thrust force is found to be smaller for linearly converging beam (LCB) and larger for linearly diverging beam (LDB) as compared to its value for uniform beam. Moreover, the virtual mass incremental factor ratio Π defined as the ratio of the kinetic energies of the beam due to added mass effect with fluid and maximum kinetic energy of the beam is computed from using the Eq. (20) and shown in Figs. 8(b), and (e). At both values of β, Π is found to be lower for higher aspect ratio. To finally observe the influence of added mass effect on frequency, the resonance frequency of the beam in air, ω_f, is compared with the frequency in vacuum, ω_v, for different tapering parameter η at $\beta = 10$ and 1000 as shown in Figs. 8(c) and (f) with $\rho b_0/\rho_b h = 0.0226$. For both the values of $\beta = 10$ and 1000, the frequency ratio ω_f/ω_v reduces for diverging beams and

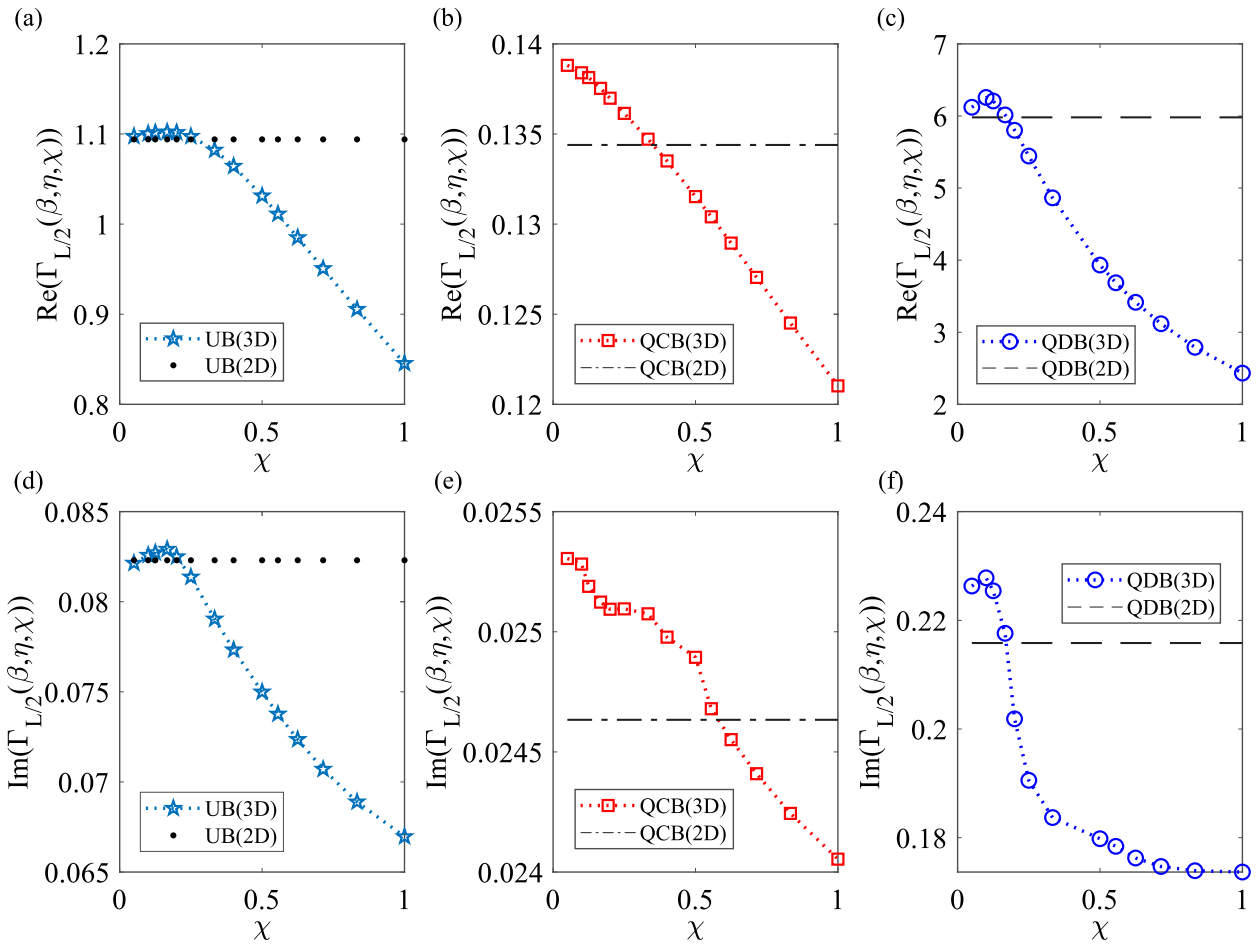

Fig. 9. Quartic hydrodynamic function is varying with the increasing aspect ratio from 0.05 to 1. The comparison of three dimensional non-uniform beam hydrodynamic function at $\beta = 1000$ at mid location of the NUB with long TBT (2D) with black different lines under consideration of tapering parameter. Plots (a), (b) and (c) denotes the added mass coefficient, and (d), (e) and (f) damping coefficient for UB($\eta = 0$,star), LCB($\eta = -0.5$,square), and LDB ($\eta = 0.5$,circle).

increases for converging beam due for all the aspect ratios. However, it is more for the larger aspect ratio of the beam. It is due to the more entrapment of fluid in the diverging beam with higher aspect ratio.

4.2. Quartic converging and diverging beam

In this section, 3D and 2D flow models are used for the computation of hydrodynamic function on a vibrating quartic converging and diverging beam in its first bending modes. The hydrodynamic function is found to be the function of frequency parameter β, tapering parameter η and aspect ratio χ. At $\beta = 1000$ and tapering parameter η(0,−0.5 and 0.5), the hydrodynamic function is evaluated at $x = L/2$ for various aspect ratio i.e., $\chi \in [0.05, 1]$. The results obtained by 3D flow model are compared with 2D flow model at various χ for uniform beam (UB), quartic converging beam (QCB) and quartic diverging beam (QDB) as shown in Figs. 9(a)–(f). The results associated with uniform have already been described in Section 4.1.

The real and imaginary components of hydrodynamic function of QCB are shown in Fig. 9(b) and (e), respectively. The real and imaginary components of hydrodynamic function computed using 3D flow model are deviated w.r.t. 2D flow model at $\chi = 0.3$ and 0.5 with a magnitude of 0.134 and 0.0247, respectively. For $\chi = 1$, the percentage difference between real and imaginary components are nearly 11% and 4%. Similarly at $\chi = 0.05$, both quantities are having a percentage difference of 4%. The percentage deviation of the real and imaginary components at both the extreme cases of the χ are below 11%, thus, it gives an allowable range for the computation of long beam model (2D) in case of quartic converging beams. Subsequently, the real and imaginary components of hydrodynamic function on quartic diverging beams are analyzed in Fig. 9(c) and (f). The components computed using the 3D flow model deviate from 2D flow model results 6.014 and 0.216, respectively, at $\chi = 0.17$. At $\chi = 1$, percentage difference of the both real and imaginary components are 146% and 24%. At $\chi = 0.05$, percentage difference of the both the components are 2.3% and 4%. The maximum peak is observed at $\chi = 0.1$ for real and imaginary component of hydrodynamic function with 5% difference. Thus, we state that 2D flow model starts deviating from $\chi = 0.17$ onward.

To investigate influence of frequency, the real and imaginary components of hydrodynamic function of UB, QCB and QDB are obtained for the frequency parameter varying from 1 to 1000. Here, 3D flow model is used with $\chi = 0.1$ and compared with 2D flow model over the above range of β range. Figs. 10(a) and (c) represent the real and imaginary hydrodynamic functions at $x = L/2$ for UB ($\chi = 0$), QCB ($\chi = -0.5$) and QDB ($\chi = -0.5$). The hydrodynamic function of 3D model follow the same pattern of 2D flow model for UB, QCB and QDB, and the result given by Sader [12] for rigid motion of UB over different frequency parameter. The real component of hydrodynamic function which is proportional to added mass effect of QCB with $\chi = 0.1$ vary from 0.86 to 0.135 with β value from 1 to 1000 as shown in Fig. 10(a). The values for QCB are found to be less than those for UB with percentage difference of 73% and 88% at $\beta = 1$ and 1000, respectively. Similarly, the values of QDB are found to be 11.61 to 6.26 over the range of β with percentage difference of 263% at $\beta = 1$ and 469% at $\beta = 1000$ when compared with the corresponding values of UB. Similarly,

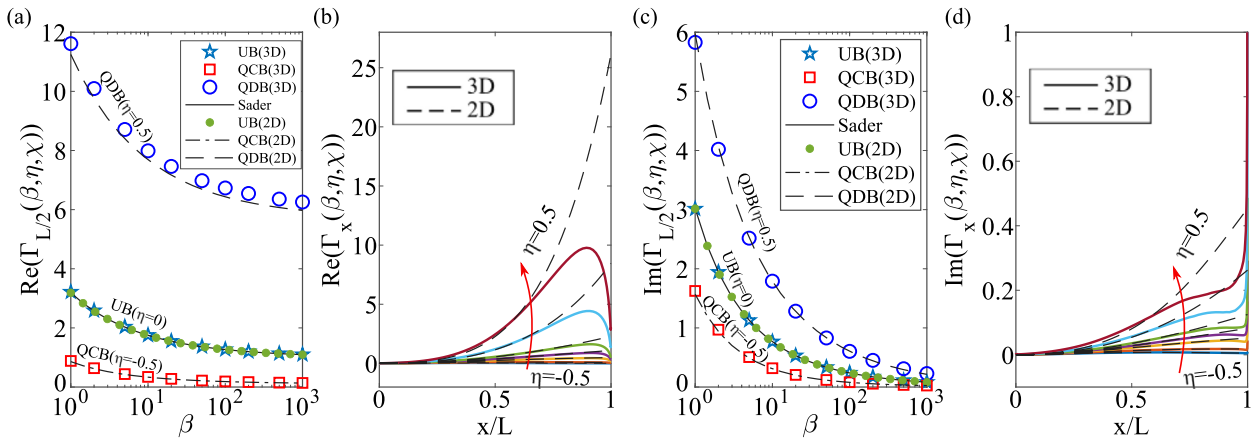

Fig. 10. The variation of quartic hydrodynamic function is with respect to the frequency parameter β and along the non-dimensional length of the beam $\xi_1 = x/L$, (a) represents the real part of the hydrodynamic function in 3D (colored shaped marker) and 2D (black solid/dashed lines) w.r.t., β at the mid location of the beam while it is in rigid oscillation at $\chi = 1/10$, (b) denotes the real part of $\Gamma_x(\beta, \eta, \chi)$ along the length of the beam at exact modeshape of NUB at $\chi = 1/10$ and $\beta = 1000$ with increasing tapering parameter η, −0.5 (LCB) to 0.5 (LDB) of a 3D (solid colored lines) and 2D (dashed black lines), (c) represents the imaginary part of the hydrodynamic function in 3D (colored shaped marker) and 2D (black solid/dashed lines) w.r.t., β at the mid location of the beam while it is in rigid oscillation at $\chi = 1/10$, (d) denotes the imaginary part of $\Gamma_x(\beta, \eta, \chi)$ along the length of the beam at exact modeshape of NUB at $\chi = 1/10$ and $\beta = 1000$ with increasing tapering parameter η, −0.5 (LCB) to 0.5 (LDB) of a 3D (solid colored lines) and 2D (dashed black lines).

the imaginary component which is proportional to damping effect for the quartic converging and diverging beam is shown in Fig. 10(c). The values for QCB are found to be less than those for UB with percentage difference of 46% and 70% at $\beta = 1$ and 1000, respectively. The values of QDB are found to be 5.83 to 0.23 over the range of β with percentage difference of 52% at $\beta = 1$ and 93% at $\beta = 1000$ when compared with the corresponding values of UB. Additionally, when the results are compared with those of linearly converging beam, the real and imaginary components of the hydrodynamic function for the QCB are found to be 60% and 34% lower at $\beta = 1$. While, these differences are 79% and 58% at $\beta = 1000$. When comparing the results with linearly diverging beam, the real and imaginary components of the hydrodynamic functions are found higher with percentage difference of 168% and 70% at $\beta = 1$ and 272% and 119% at $\beta = 1000$. The quartic diverging beam oscillating in fluid produces more added mass and damping coefficients at lower β due to the large viscous layer. Since, the vortex generation near the edge of the beam is more at higher β and the surface area of the quartic diverging beam is much more than the other beam, it produce a large added mass and damping effects. Further, we analyze the variation of hydrodynamic function along the length of the beam in terms of 2D and 3D flow below.

To understand the limitation of 2D model, we compared the local hydrodynamic function based on 3D and 2D models as a function of length of the quartic converging and diverging beam at $\chi = 0.1$ and $\beta = 1000$ as shown in Figs. 10(b) and (d). The results show that the 3D model deviates from 2D model beyond $x/L = 0.6$ and also give lower value a compared to 2D model for all values of tapering parameter. The nature of variation is found to be same as that for the LCB and LDB. Like linearly varying beam, non-linear vortex shedding effects at the trailing end of the beam is captured effectively by the 3D model. Thus, it directly influences the quality factor and resonance frequency shift.

4.2.1. Energy loss, damping ratio and quality factor

To compute the energy dissipation in converging and diverging quartic beams due to hydrodynamic effect, the product of velocity and stress jump is calculated across the quartic surface of NUB over a cycle as given by Eq. (16). for various frequency parameters β and aspect ratios χ. The ratio of energy loss ΔE to $(\mu^2\delta^2/\rho b_0)$ as a function of tapering parameter η for different values of aspect ratio χ as shown in Fig. 11(a) and (d) at $\beta = 10$ and 1000. At $\beta = 1000$, the magnitude of the energy loss ratio is three orders of magnitude more than at $\beta = 10$. The energy dissipation is also found to be higher for aspect ratio of 0.1 than with that for a larger aspect ratio. Owing to the large surface area of quartic diverging beam, energy losses are higher than with the quartic converging beam.

The damping factor is also computed using Eq. (17) which takes into account the energy loss and maximum kinetic energy of the quartic NUB. The variation of damping ratio is shown for a given value of $(\rho b_0/\rho_b h)$ in Figs. 11(b) and (e) at different $\beta = 10$ and 1000, respectively. As the tapering value is increased from −0.5 to 0.5, the damping ratio appears to be higher for the long beam, i.e., $\chi = 0.1$. For a quartic converging and diverging beam, the damping ratio decrease as the frequency parameter and aspect ratio increase. The quartic diverging beam has a higher damping ratio than the quartic converging beam for given β and χ. Further, the corresponding quality factor is also calculated for the quartic NUB as shown in Fig. 11(c), and (f) for different β and χ. It is found that higher values of aspect ratio and frequency parameter, the quality factor of converging beam increases significantly by around 13% for quartic converging beam with $\eta = -0.5$.

4.2.2. Hydrodynamic mean thrust and virtual added mass factor

Similarly, to describe the influence of tapering parameters of quartic converging and diverging beams on added (or virtual) mass effect, we compute the thrust force in terms of the frequency parameter β, the aspect ratio χ, and the tapering parameter η. It is also noticed that the coefficient $\mathcal{K}$ can alone be computed to estimate the mean thrust on the oscillating structure both theoretically [64] and numerically [19]. The coefficients $\mathcal{K}$ are computed using the imaginary component of the stress jump and the normal vector on the NUB surface for a given frequency parameter β, tapering parameter η, and aspect ratio χ. At $\beta = 10$ and $\chi = 0.1$, $\mathcal{K}$ are found to be 0.0017, 0.20, and 7.51 for tapering parameters −0.5, 0, and 0.5, respectively. At $\beta = 1000$ and $\chi = 0.1$, the coefficients $\mathcal{K}$ for QCB($\eta = -0.5$), UB($\eta = 0$), and QDB($\eta = -0.5$) are found as 0.0007, 0.13, and 5.98, respectively. As the frequency parameter increases, the coefficient $\mathcal{K}$ is decreased.

Using $\mathcal{K}$ coefficients, we calculate the mean thrust per μ^2/ρ on the NUB at $\beta = 10$ and 1000 for a given aspect ratio and tapering parameter. The variation of mean hydrodynamic thrust versus the Reynolds number over 10^{-5} to 10^5 are shown in Fig. 12(a) and (d) for a beam with aspect ratio of $\chi = 0.1$. The computed values are found to be in close agreement with the results for uniform beam given in literature [19,25] within 2% percentage error. Its value are found to be less for QCB and more for QDB than that for UB. Using the mean thrust

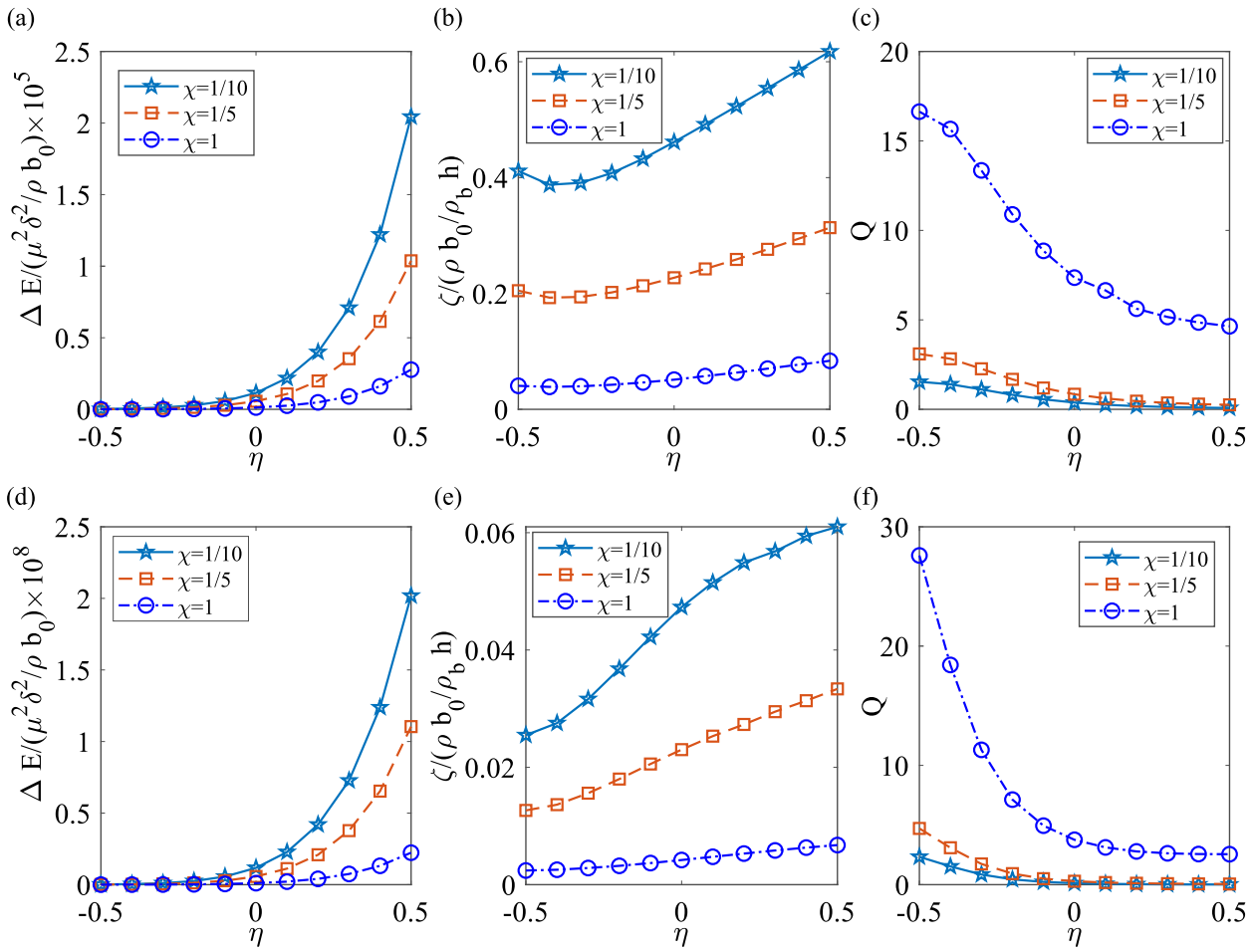

Fig. 11. The effect of the tapering parameter of quartic converging and diverging beam (−0.5 to 0.5) on the energy loss ΔE, damping ratio ζ and quality factor Q. The plots (a), (b), and (c) are the energy loss, damping ratio, and quality factor at $\beta = 10$ at various aspect ratios, i.e., $\chi = 0.1, 0.2, 1$, respectively. And the plots (d), (e), and (f) are the energy loss, damping ratio, and quality factor at $\beta = 1000$ at various aspect ratios, i.e., $\chi = 0.1, 0.2, 1$, respectively.

force, the virtual mass incremental factor ratio Π defined as the ratio of kinetic energy of beam oscillating in fluid to the maximum kinetic energy of beam is computed using Eq. (20) as shown in Figs. 12(b), and (e). It is found that the virtual mass incremental factor for the given aspect ratio and frequency parameter increases from converging to diverging beams due to increase in amount of fluid in contact. For the tapering parameter $\eta = 0.5$, virtual added mass decreases with increase in aspect ratio, χ. Finally, the influence of virtual added mass effect is shown on the ratio of beam frequency in fluid and that in vacuum for different quartic converging and diverging beams at $\beta = 10$ and 1000 as shown in Fig. 12(c), and (f). It shows that the frequency ratio is larger for structure with higher aspect ratio. Furthermore, it reduces with tapering parameter ν from −0.5 (QCB) to 0.5 (QDB) for different frequency parameters.

Finally, based on the analysis presented in the paper, quartic converging beam is found to be of higher quality factor and also low variability in frequency due to virtual added mass effect. To understand the physics we further perform numerical analysis using FEM based ANSYS software in the subsequent section.

4.3. Numerical modeling and analysis

In this section, a finite element based ANSYS software is used to calculate the hydrodynamic force on a non-uniform beam (NUB). The geometric dimension of the beam and domain are taken as follow [39,54]: length $L = 200$ μm, thickness $t = 0.965$ μm and width at the fixed end as $b_0 = 40$ μm. NUB has varying widths along the length. The fluid domain boundaries are 80 μm far away from all the surfaces of the beam such that pressure variation becomes invariable. The NUB oscillates at the exact mode shape describing the displacement and velocity boundary condition on the vibrating surface. The zero pressure condition is taken at the far-field boundary. Initially, the stationary fluid around the beam is considered as the air with density $\rho_f = 1.2$ kg/m^3 and viscosity $\mu = 1.8 \times 10^{-5}$ kg/m-s at temperature $T = 273$ ^{o}K. The flow due to the oscillating structure is treated as incompressible, viscous and isothermal under continuum regime. The unstructured 3D tetrahedral FLUID 142 elements are used to mesh the fluid domain. The sufficient refinement is done near the oscillating beam surface to predict the accurate results. The number of elements is varied from 9.53×10^5 to 13.87×10^5 for beam with uniform to quartic diverging widths. To obtain the numerical solution, the complete Navier Stokes equations is numerically solved using the commercial software ANSYS by considering the no-slip condition at the surface of the beam, and the far field is treated as outflow. Furthermore, in order to obtain steady solution, the numerical simulation is performed up to the five number of cycles. The 20 number of time steps for each cycle and a global staggered iteration of 10 are taken to obtain converged values of pressure and velocities. The arbitrary Lagrangian and Eulerian (ALE) method is activated to update the moving mesh. The pressure based transient solution is obtained using SIMPLE scheme in ANSYS. The standard $k-\epsilon$ turbulence model and second order up wind scheme is used in the solver to estimate the velocity and pressure. After obtaining the steady-state solution, we integrate the pressure and shear stress on the surface of NUB to get the hydrodynamic drag force [54].

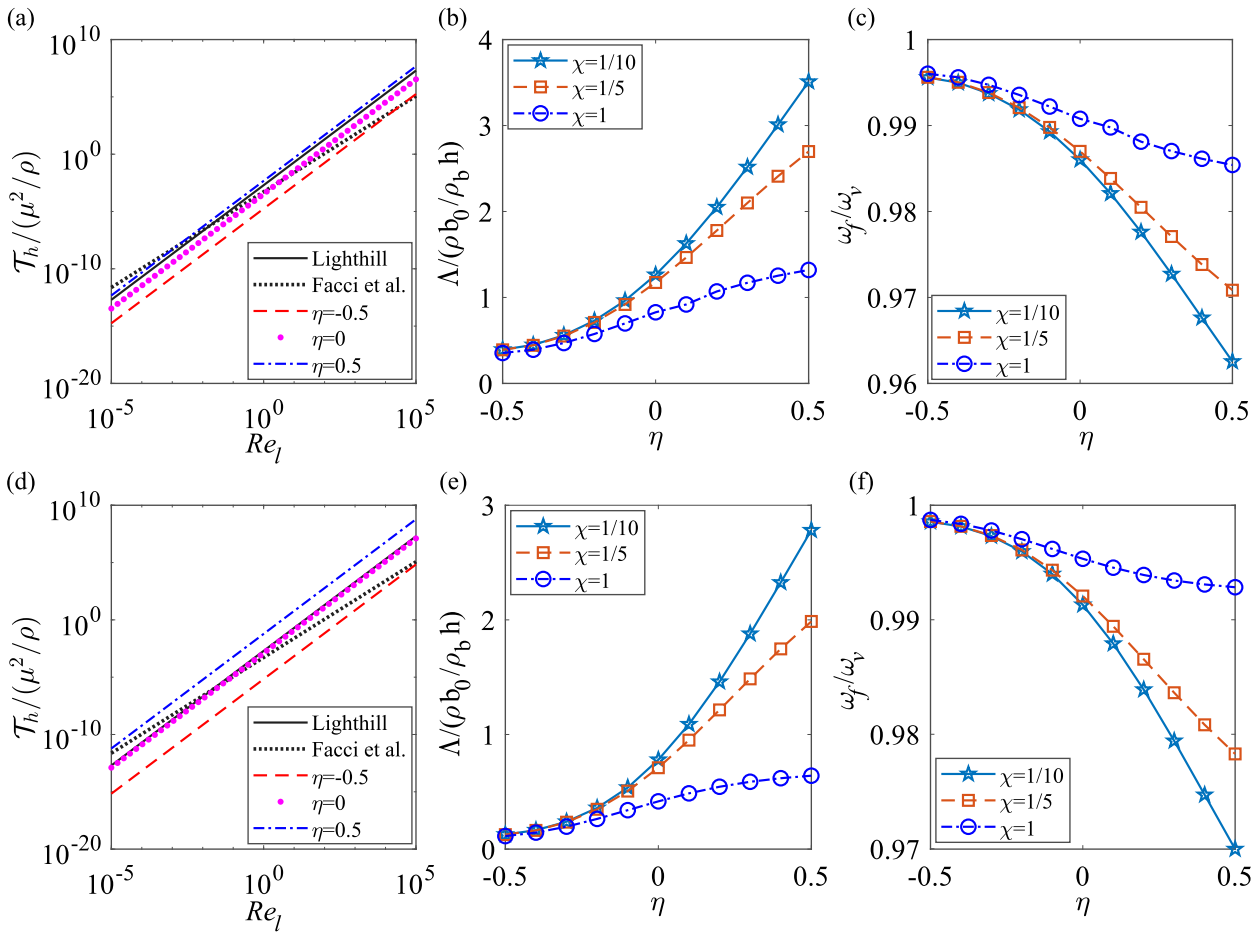

Fig. 12. The quartic hydrodynamic thrust force ratio on the NUB at extreme tapering parameter i.e., $\eta = -0.5, 0, 0.5$ with respect to the Re_l for a $\chi = 1/10$, (a), and (d) represents at $\beta = 10$, and 1000, respectively. The virtual added mass factor Λ of the beam with varying the tapering parameter η from −0.5 to 0.5(b), and (e) are representing the Λ at $\beta = 10$, and 1000 at various aspect ratio $\chi = 0.1, 0.2\&1$, respectively. Plots (c) and (f) represents the frequency ratio at $\beta = 10$ and 1000 for various η from −0.5 to 0.5 at various aspect ratio $\chi = 0.1, 0.2\&1$.

To show the pressure and velocity variation along the length of the non-uniform beam and with time about a section, we show the pressure and velocity contours in Figs. 13 for a given frequency β. The flexible non-uniform beam resonator oscillates at its fundamental first mode. The maximum displacement and velocity are at free end of the non-uniform cantilever. We considered the fluid domain such that there is no side wall effect and boundary effects as shown in Fig. 13(a). The velocity contour is shown in the plane parallel to YZ at off-set distant of $x = 0.875L$ from the fixed end. The velocity and hydrodynamic force are shown in Fig. 13(b). The transient response of the NUB is represented at $\beta = 100$ with a time period of oscillation as $T = 5.333 \times 10^{-6}$ s. We considered the sufficient number cycles to obtain steady state solution. All the pressure and velocity contour frames are drawn at maximum peak of the last cycle of force and velocity, respectively. The maximum peak of force and velocity peaks are at 4.533×10^{-6} s and 4.8×10^{-6} s. The side and top view of the pressure contours of a uniform beam denotes that the maximum pressure is at $x = 0.875L$ as shown in Fig. 13(c). The different frames parallel to YZ-plane of a NUB at $x = 0.875L$ location at $\beta = 100$ and time 4.533×10^{-6} s are also shown. We observed that with increase in the beam width, the net pressure distribution increases significantly due to the increase in the effective surface area. We also show the velocity contours of different beams at a prescribed location corresponding to the peak of the last cycle of velocity as shown in Fig. 13(d). An increases in the beam width leads to a large vortex shedding near the edges. Thus, vortex shedding formation around the beam is not only due to the amplitude of oscillation and higher frequency but also with the variation of width. The velocity contours of the uniform beam at $\beta = 100$ and $x = 0.875L$ is shown in Fig. 13(e) corresponding to a peak over last cycle from 0.85T to 0.9T. We observed that there is significant increase in the vortex formation near the edges and which reaches maximum at 0.9T. Finally, using the time difference between the force and velocity curves, i.e., dt in the last cycle, the phase difference is found as $\phi = \omega dt$. The hydrodynamic force in phase with the velocity is given as $F_{max} \cos\phi$ and that out-of-phase with the displacement/acceleration is given $F_{max} \in \phi$, where F_{max} is maximum peak force in the last cycle. Finally, the average numerical values of the hydrodynamic function are computed from the damping and inertial forces using the Eq. (13). The average added mass and damping coefficients are tabulated in Table 4 for various β of NUB.

The comparison of the average hydrodynamic function of a three-dimensional semi-analytical model with the numerical solution is represented in Table 4. The percentage deviation of the added mass and damping coefficients with respect to analytical model using 3D model are compared for $\beta = 10$ and 100. The added mass coefficient has the maximum percentage error with respect to the numerical result for the quartic diverging beam at $\eta = 0.3$ for both frequency parameters. At lower β, the hydrodynamic function obtained from the numerical model is comparatively smaller than a 3D model. On the other hand, with the higher β, the numerically computed average hydrodynamic function is significantly greater than that obtained using the 3D model. It is due to the generation of the vorticity generation around the beam edge at larger β.

We also present the comparison of absolute hydrodynamic drag force with 3D and numerical model in Fig. 14. Fig. 14(a) represents

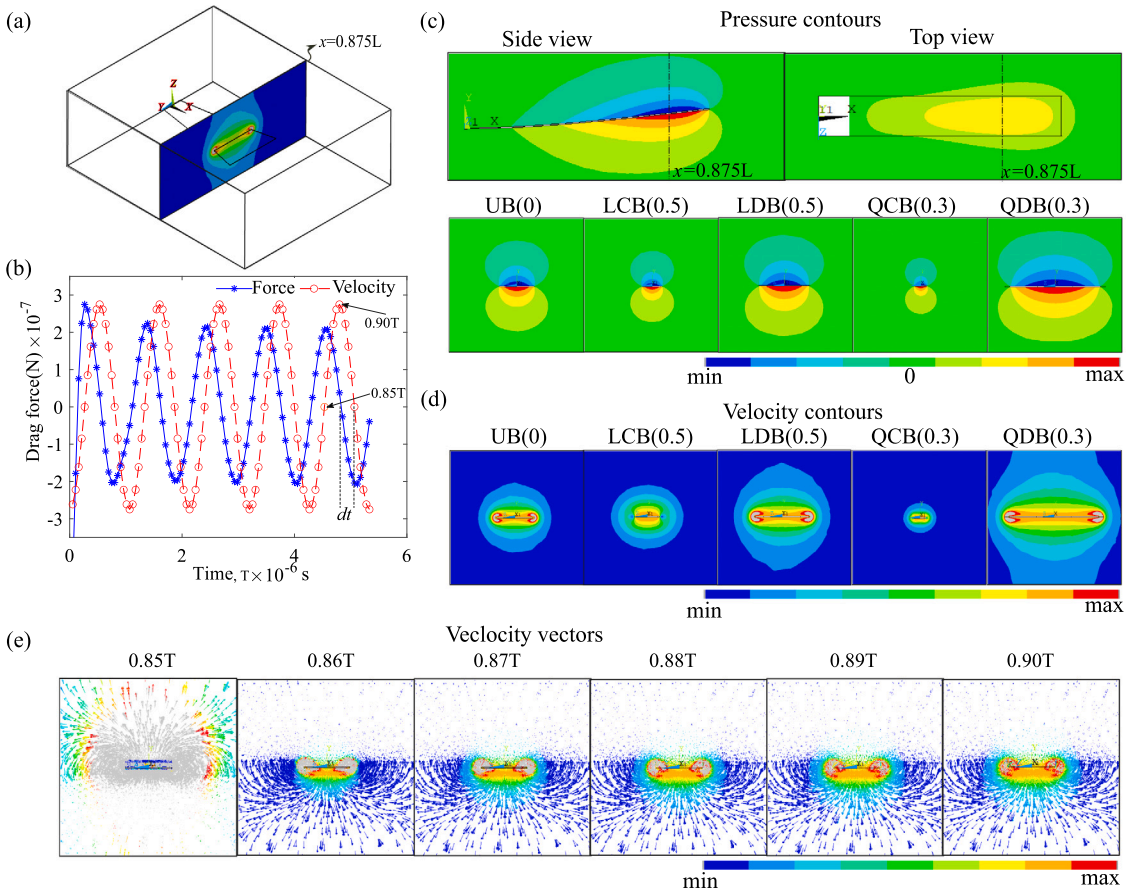

Fig. 13. (a) The numerical domain around NUB with a sufficient far boundaries at $\beta = 100$ and all front frames are presented at $x = 0.875L$. (b) denotes transient response of a ANSYS model at $\beta = 100$ up to five number of cycles which reaches to steady state response. (c) represents pressure contours at $\beta = 100$ on the surface of the uniform beam with along length, side view and top view. The frames of pressure contours at $x = 0.875L$ on different NUB(η), i.e., UB(0), LCB(0.5), LDB(0.5), QCB(0.3) and QDB(0.3) at last cycle peak. (d) represents the velocity contours of the various NUB at $\beta = 100$ at last peak. (e) denotes the velocity vectors of a uniform beam at $x = 0.875L$ at last stead state cycle reaching form 0.85T to 0.9T at $x = 0.875L$.

Table 4
The comparison of average hydrodynamic function of a 3D model with numerical model with different NUB.

η	$\beta = 10$						$\beta = 100$					
	$\mathrm{Im}(\Gamma_{\mathrm{avg}})$			$\mathrm{Re}(\Gamma_{\mathrm{avg}})$			$\mathrm{Im}(\Gamma_{\mathrm{avg}})$			$\mathrm{Re}(\Gamma_{\mathrm{avg}})$		
	3D	Num.	%err.	3D	Num.	%err.	3D	Num.	% err.	3D	Num.	%err.
UB(0)	0.289	0.256	11.4	0.619	0.611	1.3	0.088	0.093	5.68	0.443	0.486	9.7
LCB(−0.5)	0.145	0.129	11.0	0.241	0.234	2.9	0.042	0.041	2.3	0.160	0.171	6.8
LDB(0.5)	0.460	0.403	12.3	1.171	1.161	0.85	0.150	0.151	0.67	0.880	0.998	13.4
QCB(−0.3)	0.073	0.072	1.36	0.092	0.109	18.4	0.019	0.021	10.52	0.055	0.074	34.5
QDB(0.3)	1.001	0.840	16.0	3.190	3.177	0.4	0.324	0.397	22.5	2.528	2.997	18.5

the drag force with respect to wide range of the frequency parameter β starting from 1 to 1000. The analytical and numerical models provide the same trend up to the $\beta = 150$. Near $\beta = 150$, the numerical model shows a jump due to vortex shedding which is captured by the non-linear convective inertial term. The linearly converging beam has a lower drag force than that of UB or LDB for a given β. Similarly, the drag force in quartic NUB is shown in Fig. 14(b). The numerical values of absolute drag force follow the same magnitude up to $\beta = 150$ before jumping to higher value due to vortex shedding effects. Such effects are large in QCB and QDB as compared to that in linearly varying beam.

Thus, the comparison between analytical and numerical results show that 3D model developed in this paper based on unsteady Stokes equation without considering convective terms captures the damping and added mass effects in non-uniform beams correctly over a large range of frequency. However, it is unable to capture jumps as observed in numerical solution due to convective inertial effects especially in case of quartic diverging beams. Though, further improvement in the model is needed to capture convective effects, developed model can be the basis for computing drag forces in beams with different types of irregular shape employed in AFM.

5. Conclusion

The 3D BEM is applied for the first time for computing hydrodynamic forces in non-uniform flexible beams. The variation of hydrodynamic forces and corresponding effects on damping and added mass are performed in terms of frequency parameter β, aspect ratio χ and tapering parameter η. After validating the results with existing literature and comparing 3D BEM results with 2D BEM, it is found that 2D flow model can be used effectively if the aspect ratio is in the range of 0.2–0.3, i.e., for long beam. Based on the analysis of damping and added mass effect using 3D flow model, it is found that converging quartic beam gives high quality factor (less damping) and

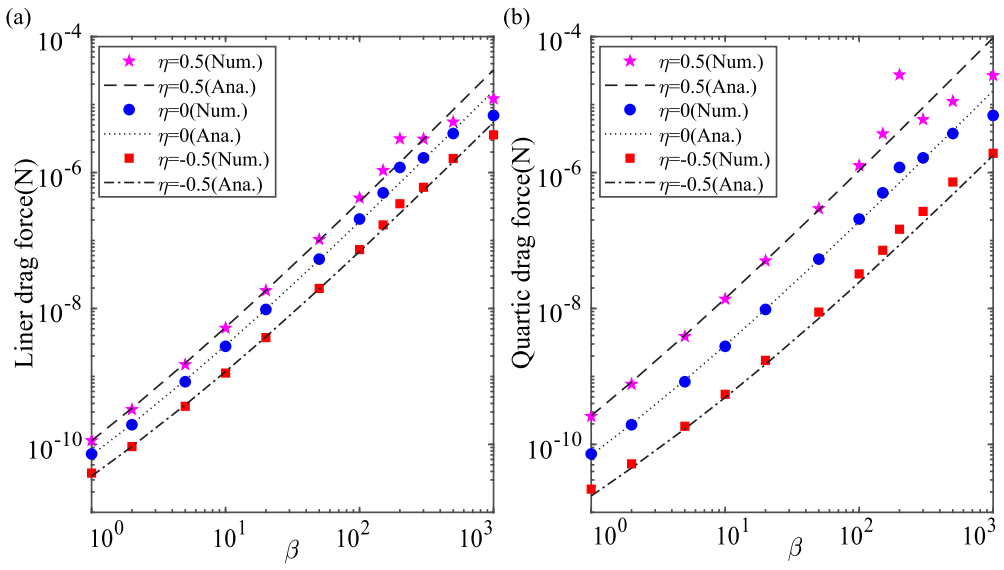

Fig. 14. The absolute value hydrodynamic drag force of a semi-analytical (black different lines) and numerical (discrete colored labels) comparison with respect to the frequency parameter β varies form 1 to 1000, (a) linear and (b) quartic converging, uniform and diverging beam.

low added mass effect due to hydrodynamic effects. As the frequency increases, quality factor increases further and added mass effect also remain relative low for quartic beam with tapering parameter of −0.5. Moreover, since the current study is limited to the computation of hydrodynamic forces in the first bending mode of non-uniform beam, the same formulation can be used to compute hydrodynamic forces corresponding to higher modes of non-uniform beam with linear and quartic varying widths.

To found the limitation of the model, results from 3D flow model is compared with numerical results from ANSYS. It is found that vortex shedding effects dominates due to convective inertial effects especially in quartic diverging beam near its resonance frequency in air. Since, the present model fails to capture this effect, further improvement in the solution can be obtained by including convective inertial terms in governing equation.

Declaration of competing interest

The authors declare that they have no known competing financial interests or personal relationships that could have appeared to influence the work reported in this paper.

Data availability

Data will be made available on request.

Acknowledgments

The first author would like to acknowledge the fellowship provided by the Ministry of Education, New Delhi, India. The work is partially supported by DRDO, New Delhi, India for funding the research work through the grant number DRDO/./IITHRC-011

Appendix A. Beam deformation due to fluid

The Euler–Bernoulli beam equation is written for the representation of the non-uniform beam denotes width is varying along the length. The boundary conditions of a cantilever beam are at fixed support sloe and deflections are zero and at free end location the shear and moments are zero.

$$m_s(x)\frac{\partial^2 W(x,t)}{\partial t^2} + \frac{\partial^2}{\partial x^2}\left(EI(x)\frac{\partial^2 W(x,t)}{\partial x^2}\right) = F(x,t), \tag{A.1}$$

$$W(x,t)|_{x=0} = \frac{\partial W(x,t)}{\partial x}\bigg|_{x=0} = EI(x)\frac{\partial^2 W(x,t)}{\partial x^2}\bigg|_{x=L} = \frac{\partial}{\partial x}\left(EI(x)\frac{\partial^2 W(x,t)}{\partial x^2}\right)\bigg|_{x=L} = 0. \tag{A.2}$$

Appendix B. Incomprehensible unsteady Stokes equation in fluid

The small amplitude of oscillation of the beam describes unsteady Stokes equation which neglects the convective enteral force term in the complete Navier Stokes equation and there is no gravity force. The continuity and linearized momentum equations are written as

$$\nabla \cdot \bar{\boldsymbol{u}}(x,y,z,t) = 0; \tag{B.1a}$$

$$\rho\frac{\partial \bar{\boldsymbol{u}}(x,y,z,t)}{\partial t} = -\nabla p(x,y,z,t) + \mu\nabla^2\bar{\boldsymbol{u}}(x,y,z,t). \tag{B.1b}$$

References

[1] Hosaka H, Itao K, Kuroda S. Damping characteristics of beam-shaped micro-oscillators. Sens Actuator A Phys 1995;49(1–2):87–95. http://dx.doi.org/10.1016/0924-4247(95)01003-J.

[2] Korayem A, Imani F, Korayem M. Modeling the amplitude mode of piezoelectric microcantilever afm in contrast to the surface of the sample in a liquid medium. Arab J Sci Eng 2020;40(2):675–88. http://dx.doi.org/10.1007/s13369-019-04129-6.

[3] Xiu H, Davis RB, Romeo RC. Edge clearance effects on the added mass and damping of beams submerged in viscous fluids. J Fluids Struct 2018;83:194–217. http://dx.doi.org/10.1016/j.jfluidstructs.2018.08.016.

[4] Abdelnour K, Mancia E, Peterson SD, Porfiri M. Hydrodynamics of underwater propulsors based on ionic polymer–metal composites: a numerical study. Smart Mater Struct 2009;18(8):085006. http://dx.doi.org/10.1088/0964-1726/18/8/085006.

[5] Dufour I, Lemaire E, Caillard B, Debeda H, Lucat C, Heinrich SM, et al. Effect of hydrodynamic force on microcantilever vibrations: Applications to liquid-phase chemical sensing. Sens Actuators B Chem 2009;18(8):085006. http://dx.doi.org/10.1016/j.snb.2013.10.106.

[6] Riesch C, Reichel EK, Keplinger F, Jakoby B. Characterizing vibrating cantilevers for liquid viscosity and density sensing. J Sens 2008. http://dx.doi.org/10.1155/2008/697062.

[7] Aureli M, Basaran ME, Porfiri M. Nonlinear finite amplitude vibrations of sharp-edged beams in viscous fluids. J Sound Vib 2012;331(7):1624–54. http://dx.doi.org/10.1016/j.jsv.2011.12.007.

[8] Ahsan SN, Aureli M. Nonlinear oscillations of shape-morphing submerged structures: Control of hydrodynamic forces and power dissipation via active flexibility. J Fluids Struct 2017;74:35–52. http://dx.doi.org/10.1016/j.jfluidstructs.2017.06.010.

[9] Ma S, Bai H, Wang S, Zhao L, Yang K, Fang R, et al. Detecting the mass and position of a particle by the vibration of a cantilevered micro-plate. Int J Mech Sci 2020;172:105413. http://dx.doi.org/10.1016/j.ijmecsci.2019.105413.
[10] Ma S, Li M, Wang S, Liu H, Wang H, Ren L, et al. Multiple particle identification by sequential frequency-shift measurement of a micro-plate. Int J Mech Sci 2022;231:107587. http://dx.doi.org/10.1016/j.ijmecsci.2022.107587.
[11] Koens L, Montenegro-Johnson TD. Local drag of a slender rod parallel to a plane wall in a viscous fluid. Phys Rev Fluids 2021;6(6):064101. http://dx.doi.org/10.1103/PhysRevFluids.6.064101.
[12] Sader JE. Frequency response of cantilever beams immersed in viscous fluids with applications to the atomic force microscope. J Appl Phys 1998;84(1):64–76. http://dx.doi.org/10.1063/1.368002.
[13] Sader JE, Sanelli JA, Adamson BD, Monty JP, Wei X, Crawford SA, et al. Spring constant calibration of atomic force microscope cantilevers of arbitrary shape. Rev Sci Instrum 2012;83(10):103705. http://dx.doi.org/10.1063/1.4757398.
[14] Sader JE, Friend JR. Note: Calibration of atomic force microscope cantilevers using only their resonant frequency and quality factor. Rev Sci Instrum 2014;85(11):16101. http://dx.doi.org/10.1063/1.4901227.
[15] Green CP, Sader JE. Frequency response of cantilever beams immersed in viscous fluids near a solid surface with applications to the atomic force microscope. J Appl Phys 2005;98(11):114913. http://dx.doi.org/10.1063/1.2136418.
[16] Korayem AH, Korayem MH. Effect of three types of piezoelectric cantilever on the topography quality in the vicinity of rough surface in a fluid ambient. Appl Math Model 2019;65:333–47. http://dx.doi.org/10.1016/j.apm.2018.08.034.
[17] Van Eysden CA, Sader JE. Small amplitude oscillations of a flexible thin blade in a viscous fluid: Exact analytical solution. Phys Fluids 2006;18(12):123102. http://dx.doi.org/10.1063/1.2395967.
[18] Singh SS, Pal P, Pandey AK. Pull-in analysis of non-uniform microcantilever beams under large deflection. J Appl Phys 2015;118(20):204303. http://dx.doi.org/10.1063/1.4936321.
[19] Facci AL, Porfiri M. Analysis of three-dimensional effects in oscillating cantilevers immersed in viscous fluids. J Fluids Struct 2013;38:205–22. http://dx.doi.org/10.1016/j.jfluidstructs.2012.11.006.
[20] Sahoo DK, Pandey AK. Performance of non-uniform cantilever based piezoelectric energy harvester. ISSS J Micro Smart Syst 2018;7(1):1–13. http://dx.doi.org/10.1007/s41683-018-0018-2.
[21] Syed WU, Bojesomo A, Elfadel IM. Electromechanical model of a tapered piezoelectric energy harvester. IEEE Sens J 2018;18(14):5853–62. http://dx.doi.org/10.1109/JSEN.2018.2841359.
[22] Vazquez J, Rivera MA, Hernando J, Sanchez-Rojas JL. Dynamic response of low aspect ratio piezoelectric microcantilevers actuated in different liquid environments. J Micromech Microeng 2008;19(1):015020. http://dx.doi.org/10.1088/0960-1317/19/1/015020.
[23] Wang J, Zhang C, Zhang M, Abdelkefi A, Yu H, Ge X, et al. Enhancing energy harvesting from flow-induced vibrations of a circular cylinder using a downstream rectangular plate: An experimental study. Int J Mech Sci 2021;211:106781. http://dx.doi.org/10.1016/j.ijmecsci.2021.106781.
[24] Shi G, Tan T, Hu S, Yan Z. Hydrodynamic piezoelectric energy harvesting with topological strong vortex by forced separation. Int J Mech Sci 2022;223:107261. http://dx.doi.org/10.1016/j.ijmecsci.2022.107261.
[25] Lighthill M, Rosenhead LE. Laminar boundary layers. USA: Oxford University Press; 1963, p. 5–88.
[26] Nuriev AN, Egorov AG, Kamalutdinov AM. Hydrodynamic forces acting on the elliptic cylinder performing high-frequency low-amplitude multi-harmonic oscillations in a viscous fluid. J Fluid Mech 2021;913. http://dx.doi.org/10.1017/jfm.2020.1180.
[27] Bidkar RA, Kimber M, Raman A, Bajaj AK, Garimella SV. Nonlinear aerodynamic damping of sharp-edged flexible beams oscillating at low Keulegan–Carpenter numbers. J Fluid Mech 2009;634:269–89. http://dx.doi.org/10.1017/S0022112009007228.
[28] Nuriev A, Kamalutdinov A, Zaitseva O. Hydrodynamics around long vibrating beams. J Fluids Struct 2021;101:103203. http://dx.doi.org/10.1016/j.jfluidstructs.2020.103203.
[29] Tafuni A, Sahin I. Non-linear hydrodynamics of thin laminae undergoing large harmonic oscillations in a viscous fluid. J Fluids Struct 2015;52:101–17. http://dx.doi.org/10.1016/j.jfluidstructs.2014.10.004.
[30] Colin M, Thomas O, Grondel S, Cattan E. Very large amplitude vibrations of flexible structures: Experimental identification and validation of a quadratic drag damping model. J Fluids Struct 2020;97:103056. http://dx.doi.org/10.1016/j.jfluidstructs.2020.103056.
[31] Aureli M, Porfiri M. Low frequency and large amplitude oscillations of cantilevers in viscous fluids. Appl Phys Lett 2010;96(16):164102. http://dx.doi.org/10.1063/1.3405720.
[32] Shrestha B, Ahsan SN, Aureli M. Experimental study of oscillating plates in viscous fluids: Qualitative and quantitative analysis of the flow physics and hydrodynamic forces. Phys Fluids 2018;30(1):013102. http://dx.doi.org/10.1063/1.5001330.
[33] Naik T, Longmire EK, Mantell SC. Dynamic response of a cantilever in liquid near a solid wall. Sens Actuators A Phys 2003;102(3):240–54. http://dx.doi.org/10.1016/S0924-4247(02)00398-9.
[34] Gesing A, Platz D, Schmid U. Viscous fluid–structure interaction of microresonators in the beam–plate transition. J Appl Phys 2022;131(13):134502. http://dx.doi.org/10.1063/5.0085514.
[35] Hu L, Yan H, Zhang WM, Zou HX, Peng ZK, Meng G. Theoretical and experimental study on dynamic characteristics of V-shaped beams immersed in viscous fluids: From small to finite amplitude. J Fluids Struct 2018;82:215–44. http://dx.doi.org/10.1016/j.jfluidstructs.2018.07.006.
[36] Basak S, Raman A, Garimella SV. Hydrodynamic loading of microcantilevers vibrating in viscous fluids. J Appl Phys 2006;99(11):114906. http://dx.doi.org/10.1063/1.2202232.
[37] Clarke RJ, Jensen OE, Billingham J, Williams PM. Three-dimensional flow due to a microcantilever oscillating near a wall: an unsteady slender-body analysis. Proc R Soc A Math Phys Eng Sci 2006;462(2067):913–33. http://dx.doi.org/10.1098/rspa.2005.1607.
[38] Clarke RJ, Jensen OE, Billingham J. Three-dimensional elastohydrodynamics of a thin plate oscillating above a wall. Phys Rev E 2008;78(5):056310. http://dx.doi.org/10.1103/PhysRevE.78.056310.
[39] Ashok A, Gangele A, Pal P, Pandey AK. An analysis of stepped trapezoidal-shaped microcantilever beams for MEMS-based devices. J Micromech Microeng 2018;28(7):075009. http://dx.doi.org/10.1088/1361-6439/aab8ac.
[40] Ashok A, Nighot RP, Sahu NK, Pal P, Pandey AK. Design and analysis of microcantilever beams based on arrow shape. Microsyst Technol 2019;25(11):4379–90. http://dx.doi.org/10.1007/s00542-019-04555-4.
[41] Alcheikh N, Ouakad HM, Younis MI. Dynamic analysis of straight stepped microbeams. Int J Non Linear Mech 2021;128:103639. http://dx.doi.org/10.1016/j.ijnonlinmec.2020.103639.
[42] Umeda N, Ishizaki S, Uwai H. Scanning attractive force microscope using photothermal vibration. J Vac Sci Technol B Microelectron Nanometer Struct Process Meas Phenom 1991;9(2):1318–22. http://dx.doi.org/10.1116/1.585187.
[43] Troesch AW, Kim SK. Hydrodynamic forces acting on cylinders oscillating at small amplitudes. J Fluids Struct 1991;5(1):113–26. http://dx.doi.org/10.1016/0889-9746(91)80014-5.
[44] Zhang W, Turner KL. Fluid damping and loading effects of MEMS flexural resonators: Theory and applications. 2006, Online publication 2006;https://www.researchgate.net.
[45] Zhang W, Turner K. Frequency dependent fluid damping of micro/nano flexural resonators: Experiment, model and analysis. Sens Actuator A Phys 2007;134(2):594–9. http://dx.doi.org/10.1016/j.sna.2006.06.010.
[46] Kanwal RP. Vibrations of an elliptic cylinder and a flat plate in a viscous fluid. Z Angew Math Mech 1955;35(1–2):17–22. http://dx.doi.org/10.1002/zamm.19550350104.
[47] Tuck EO. Calculation of unsteady flows due to small motions of cylinders in a viscous fluid. J Eng Math 1969;3(1):29–44. http://dx.doi.org/10.1007/bf01540828.
[48] Brumley DR, Willcox M, Sader JE. Oscillation of cylinders of rectangular cross section immersed in fluid. Phys Fluids 2010;22(5):052001. http://dx.doi.org/10.1063/1.3397926.
[49] Phan CN, Aureli M, Porfiri M. Finite amplitude vibrations of cantilevers of rectangular cross sections in viscous fluids. J Fluids Struct 2013;40:52–69. http://dx.doi.org/10.1016/j.ijmecsci.2013.05.011.
[50] Sader JE, Chon JW, Mulvaney P. Calibration of rectangular atomic force microscope cantilevers. Rev Sci Instrum 1999;70(10):3967–9. http://dx.doi.org/10.1063/1.1150021.
[51] Sader JE, Pacifico J, Green CP, Mulvaney P. General scaling law for stiffness measurement of small bodies with applications to the atomic force microscope. J Appl Phys 2005;97(12):124903. http://dx.doi.org/10.1063/1.1935133.
[52] Rankl C, Pastushenko V, Kienberger F, Stroh CM, Hinterdorfer P. Hydrodynamic damping of a magnetically oscillated cantilever close to a surface. Ultramicroscopy 2004;100(3–4):301–8. http://dx.doi.org/10.1016/j.ultramic.2003.12.014.
[53] Grimaldi E, Porfiri M, Soria L. Finite amplitude vibrations of a sharp-edged beam immersed in a viscous fluid near a solid surface. J Appl Phys 2012;112(10):104907. http://dx.doi.org/10.1063/1.4765029.
[54] Akarapu A, Nighot RP, Devsoth L, Yadav M, Pal P, Pandey AK. Experimental and theoretical analysis of drag forces in micromechanical-beam arrays. Phys Rev Appl 2020;13(3):034003. http://dx.doi.org/10.1103/PhysRevApplied.13.034003.
[55] Vignola JF, Judge JA, Jarzynski J, Zalalutdinov M, Houston BH, Baldwin JW. Effect of viscous loss on mechanical resonators designed for mass detection. Appl Phys Lett 2006;88(4):041921. http://dx.doi.org/10.1063/1.2165186.
[56] Ahsan SN, Aureli M. Finite amplitude torsional oscillations of shape-morphing plates immersed in viscous fluids. Phys Fluids 2020;32(5):053101. http://dx.doi.org/10.1063/1.5136256.
[57] Maali A, Hurth C, Boisgard R, Jai C, Cohen-Bouhacina T, Aimé JP. Hydrodynamics of oscillating atomic force microscopy cantilevers in viscous fluids. J Appl Phys 2005;97(7):074907. http://dx.doi.org/10.1063/1.1873060.
[58] Korayem AH, Taghizade M, Korayem MH. Sensitivity analysis of surface topography using the submerged non uniform piezoelectric micro cantilever in liquid by considering interatomic force interaction. J Mech Sci Technol 2018;32(5):2201–7. http://dx.doi.org/10.1007/s12206-018-0430-3.

[59] Pozrikidis C. A singularity method for unsteady linearized flow. Phys Fluids A Fluid Dyn 1989;1(9):1508–20. http://dx.doi.org/10.1063/1.857329.
[60] Pozrikidis C. A study of linearized oscillatory flow past particles by the boundary-integral method. J Fluid Mech 1989;202:17–41. http://dx.doi.org/10.1017/S0022112089001084.
[61] Loewenberg M. Axisymmetric unsteady Stokes flow past an oscillating finite-length cylinder. J Fluid Mech 1994;265:265–88. http://dx.doi.org/10.1017/S0022112094000832.
[62] Ahsan SN, Aureli M. Three-dimensional analysis of hydrodynamic forces and power dissipation in shape-morphing cantilevers oscillating in viscous fluids. Int J Mech Sci 2018;149:436–51. http://dx.doi.org/10.1016/j.ijmecsci.2017.09.034.
[63] Farokhi H, Ghayesh MH. Geometrically exact extreme vibrations of cantilevers. Int J Mech Sci 2020;168:105051. http://dx.doi.org/10.1016/j.ijmecsci.2019.105051.
[64] Lighthill MJ. Aquatic animal propulsion of high hydromechanical efficiency. J Fluid Mech 1970;44(2):265–301. http://dx.doi.org/10.1017/S0022112070001830.
[65] Lou J, Gu T, Chen T, Yang Y, Xu C, Wei Y, et al. Effects of actuator-substrate ratio on hydrodynamic and propulsion performances of underwater oscillating flexible structure actuated by macro fiber composites. Mech Syst Signal Process 2022;170:108824. http://dx.doi.org/10.1016/j.ymssp.2022.108824.
[66] Vishwakarma SD, Pandey AK, Parpia JM, Verbridge SS, Craighead HG, Pratap R. Size modulated transition in the fluid–structure interaction losses in nano mechanical beam resonators. J Appl Phys 2016;119(19):194303. http://dx.doi.org/10.1063/1.4950758.
[67] Ashok A, Kumar PM, Singh SS, Raju P, Pal P, Pandey AK. Achieving wideband micromechanical system using coupled non-uniform beams array. Sens Actuator A Phys 2018;273:12–8. http://dx.doi.org/10.1016/j.sna.2018.02.008.
[68] Ma C, Shao M, Ma J, Liu C, Gao K. Fluid structure interaction analysis of flexible beams vibrating in a time-varying fluid domain. Proc Inst Mech Eng C J Mech Eng Sci 2020;234(10):1913–27. http://dx.doi.org/10.1177/09544062209021.
[69] Gesing A, Platz D, Schmid U. A numerical method to determine the displacement spectrum of micro-plates in viscous fluids. Comput Struct 2022;260:106716. http://dx.doi.org/10.1016/j.compstruc.2021.106716.
[70] Basak S, Raman A. Hydrodynamic coupling between micromechanical beams oscillating in viscous fluids. Phys Fluids 2007;19(1):017105. http://dx.doi.org/10.1063/1.2423254.
[71] Intartaglia C, Soria L, Porfiri M. Hydrodynamic coupling of two sharp-edged beams vibrating in a viscous fluid. Proc R Soc A Math Phys Eng Sci 2014;470(2162):20130397. http://dx.doi.org/10.1098/rspa.2013.0397.
[72] Devsoth L, Pandey AK. Two-dimensional hydrodynamic forces in an array of shape-morphed cantilever beams. In: Conference on microactuators and micromechanisms mechan. Machine science. Vol. 126. Cham: Springer; 2023, p. 232–43. http://dx.doi.org/10.1007/978-3-031-20353-4_18.
[73] Amabili M, Kwak MK. Free vibrations of circular plates coupled with liquids: revising the lamb problem. J Fluids Struct 1996;10(7):743–61. http://dx.doi.org/10.1006/jfls.1996.0051.